



# Multiscale and monolithic arbitrary Lagrangian–Eulerian finite element method for a hemodynamic fluid–structure interaction problem involving aneurysms

Wenrui Hao<sup>a</sup>, Pengtao Sun<sup>b,\*</sup>, Jinchao Xu<sup>a</sup>, Lian Zhang<sup>a</sup>

<sup>a</sup> Department of Mathematics, Pennsylvania State University, University Park, PA, 16802, USA

<sup>b</sup> Department of Mathematical Sciences, University of Nevada Las Vegas, Las Vegas, NV, 89154, USA

## ARTICLE INFO

### Article history:

Available online 5 February 2021

### Keywords:

Hemodynamic fluid–structure interaction (FSI)  
Heterogeneous multiscale method (HMM)  
Seamless multiscale method (SMM)  
Arbitrary Lagrangian–Eulerian (ALE) mapping  
Mixed finite element method (FEM)  
Abdominal aortic aneurysms (AAA)

## ABSTRACT

In this paper, a multiscale and monolithic arbitrary Lagrangian–Eulerian finite element method (ALE-FEM) is developed for a multiscale hemodynamic fluid–structure interaction (FSI) problem involving an aortic aneurysm growth to quantitatively predict the long-term aneurysm risk in the cardiovascular environment, where the blood fluid profile, the hyperelastic arterial wall, and the aneurysm pathophysiology are integrated into one hemodynamic FSI model, together with no-slip interface conditions between the blood fluid and the arterial wall. Additionally, two different time scales are involved: a fast time scale for the blood fluid–arterial wall interaction process in terms of seconds, and a slow time scale for the biological (abdominal aortic aneurysms (AAA) progression) process in terms of years. Two types of multiscale methods, the heterogeneous multiscale method (HMM) and the seamless multiscale method (SMM), are employed to tackle different time scales while the arbitrary Lagrangian–Eulerian (ALE) method is adopted to generate the moving blood fluid meshes that adapt to the deformation of the hyperelastic arterial wall all the time, based on which the variable time-stepping/mixed finite element method (FEM) is defined in the ALE frame to discretize the developed hemodynamic FSI model involving aneurysms. A two-dimensional schematic blood fluid–artery–aneurysm interaction example and a three-dimensional realistic cardiovascular FSI problem with an aortic aneurysm growth based upon the patients' CT scan data are simulated to validate the accuracy and the efficiency of our developed HMM(SMM)/ALE-FEM, and a medically reasonable long-term prediction is obtained for the aneurysm growth as well.

© 2021 Elsevier Inc. All rights reserved.

## 1. Introduction

Abdominal aortic aneurysms (AAA) affect more than 10 million people and become one of the leading causes of death in the US [1], also cause over 175,000 deaths worldwide [2]. In clinical practice, it is important not only to treat AAA itself but also to tailor treatment to each AAA patient's disease-specific variation. This approach of treatment, known as personalized/precision medicine [3–5], is based on current understandings of the fundamental mechanisms underlying AAA and involves a combination of genomic, network-dynamic, and environmental factors. In order to study the multifactorial pathophysiology of AAA in the cardiovascular environment, proper integrative approaches have been introduced to capture

\* Corresponding author.

E-mail address: pengtao.sun@unlv.edu (P. Sun).

the interplay of its biological mechanisms and homeostatic networks. Computational modeling techniques, such as computational fluid dynamics, and more sophisticatedly, fluid-structure interactions (FSI), is one such approach that has been successfully implemented in the study of cardiovascular diseases (CVDs) and has provided many insightful suggestions for clinical practices [6–21]. However, most extant modeling techniques in AAA research focus on the short-term effects of blood fluid acting on aneurysms, without considering AAA long-term progression. This lack is due not just to the fact that AAA progression is unclear in the long term, but also to the computational challenges arising from the multiscale and multiphysics features of the blood fluid-artery interaction modeling that comprises AAA growth, where two different time scales are involved: a fast time scale for the blood fluid profile in terms of seconds, and a slow time scale for AAA growth in terms of years, in addition, the moving interface between the blood fluid and the artery is produced to account for the deformable arterial wall that interacts with the blood fluid impact all the time. Therefore, two long-standing, grand challenges are facing AAA mathematical modeling research communities: 1) modeling challenges of incorporating the pathophysiology of AAA into mathematical models of such hemodynamic FSI problem, and 2) computational challenges of developing accurate, efficient, and robust numerical methods to simulate such a strongly nonlinear and multiscale FSI problem. The lack of solutions to these grand challenges limits capabilities of mathematical modeling and numerical simulations in AAA precision medicine, including the use of pathogenesis data such as genomics, transcriptomics, and imaging. Hence there is a critical need to develop an innovative, robust, and efficient mathematical/numerical modeling approach for capturing long-term AAA progression as well as personalizing treatment for AAA patients.

In this paper, we propose a comprehensive FSI model to describe the dynamic multiphysics system of incompressible blood fluid, the incompressible and hyperelastic arterial wall, and AAA pathophysiology, among which no-slip interactions occurring through the moving interface and different time scales are involved. In principle, to model the blood fluid, we consider the Navier–Stokes equations under the assumptions of incompressibility and Newtonian rheology, which is defined in Eulerian description. The dynamic structure equation of the incompressible and hyperelastic arterial wall, which is conventionally described in Lagrangian description, can be generally defined by the constitutive relation of various hyperelastic materials, and, the blood fluid and the arterial wall exist in separate domains that are coupled along a shared moving interface and interact with each other. In addition, in such a set of governing equations of FSI problem, the time and space dependence of the primary unknowns and of the moving interfaces play a significant role in the dynamic interaction between the fluid and the structure, where we assume the no-slip interface conditions hold across the interface.

Regarding the numerical methodology to be studied in this paper, we develop multiscale and monolithic arbitrary Lagrangian–Eulerian (ALE) finite element methods (FEM) to tackle the proposed multiscale FSI model with AAA progression. In the first place, we prefer the monolithic approach [22], in view of its unconditional stability and the immunity of any systematic error in the implementation of interface conditions for any kind of FSI problem. Moreover, a high-performance preconditioning linear algebraic solver can also be developed and parallelized for the monolithic system without doing an alternating iteration by subdomains [23]. In contrast, the partitioned approach [24], which decouples the FSI system and iteratively solves the fluid and the structure equations via an iteration-by-subdomain approach, is conditionally stable and conditionally convergent under a particular range of the physical parameters of FSI model. For instance, if both fluid and structural densities are of the same order, then the so-called added-mass effect [25] will be specifically induced by the partitioned approach, resulting in an unstable and/or nonconvergent iteration. Unfortunately, the hemodynamic FSI problems are within the particular range of the added-mass effect, making the partitioned approach very difficult to converge. Hence, the monolithic approach is the primarily reliable method to be studied in this paper.

On the top of the monolithic approach, we adopt the ALE finite element method to discretize the presented FSI problem. As a type of body-fitted mesh method, ALE techniques [22,26–31] have become the most accurate and also the most popular approach for solving FSI problems and other general moving boundary/interface problems within the frame of mixed finite element approximation [32–38], where the mesh on the interface is accommodated to be shared by both the fluid and the structure, and thus to automatically satisfy the interface conditions across the interface. On the other hand, considering that the microscopic process of the presented hemodynamic FSI is in equilibrium with the unchanged local macroscopic process of AAA progression, we employ the heterogeneous multiscale method (HMM) [39] to handle the multiscale challenge by combining our fully discrete ALE-FEM with a specific variable time-stepping approach. In addition, another type of multiscale method, the seamless multiscale method (SMM) [40], is also studied and applied to the developed fully discrete ALE-FEM based on the fact that the FSI process can quickly relax to a (quasi) steady state on the microscopic time scale, in contrast to the much slower macroscopic time scale of the biological process. Thus in this paper, for the first time, we develop two types of multiscale, monolithic ALE finite element methods to simulate the proposed multiscale hemodynamic FSI model involving the aneurysm growth.

In addition, the hemodynamic FSI model to be proposed in this paper, which describes the incompressible arterial wall involving aneurysms as one kind of hyperelastic structure influenced by a biological process, can serve as a powerful tool to provide a basic description for the complex biological system presented in AAA, and, the developed numerical methodology can be applied to the clinical patients' CT scan data to finally produce a long-term prediction of AAA growth, as shown in Section 5, where a series of numerical simulations in both 2D and 3D cases are carried out to validate the presented model and the developed numerical methods. Besides that, the rest structures of the paper are given below. We introduce mathematical models of the proposed hemodynamic FSI problem involving aneurysms in Section 2, then define its weak form in the ALE frame in Section 3, following the introduction of ALE mapping. Mixed finite element spaces and

the HMM(SMM)/ALE-FEM for the presented FSI problem are defined in Section 4, followed by numerical experiments in Section 5 and a conclusion in Section 6.

## 2. Model description

We consider the FSI problem between the arterial wall, which mainly consists of the smooth muscle cells (SMCs), and the blood fluid flow. The blood fluid pressure impacts on the inner surface of the arterial wall to make it deform, while a part of the arterial wall may dramatically change its shape to get the aneurysm formed, gradually, due to the loss of elasticity therein. More specifically, we use  $\Omega_f^t = \Omega_f(t) \subset \mathbb{R}^d$  ( $d = 2, 3$ ) and  $\Omega_s(t) \subset \mathbb{R}^d$  to denote the current domain of the blood fluid and the arterial wall, respectively. Boundaries of these two domains are then denoted by  $\Gamma_f(t)$  and  $\Gamma_s(t)$ , respectively. We also denote the interface between the blood fluid and the arterial wall by  $\Gamma_I^t = \Gamma_I(t) = \Gamma_f(t) \cap \Gamma_s(t)$ . Note that the SMCs grow inside the arterial wall so that  $\Omega_s(t)$  is also the domain holding the SMCs there. In order to distinguish domains, boundaries and physical variables/parameters in the reference (Lagrangian) description from those in the current (Eulerian) description, we introduce the notation “ $\hat{\cdot}$ ”, such as  $\hat{\Omega}_f = \Omega_f(0)$ ,  $\hat{\Omega}_s = \Omega_s(0)$ ,  $\hat{\Gamma}_f = \Gamma_f(0)$ ,  $\hat{\Gamma}_s = \Gamma_s(0)$  and  $\hat{\Gamma}_I = \Gamma_I(0)$ . Corresponding to any point  $\hat{\mathbf{x}} \in \hat{\Omega} = \hat{\Omega}_f \cup \hat{\Omega}_s$ , the current position at time  $t$  is denoted by  $\mathbf{x}(\hat{\mathbf{x}}, t) \in \Omega = \Omega_f \cup \Omega_s$ . Then, the structure displacement and velocity are defined in the reference domain, as:  $\hat{\mathbf{u}}(\hat{\mathbf{x}}, t) = \mathbf{x} - \hat{\mathbf{x}}$  and  $\hat{\mathbf{v}}(\hat{\mathbf{x}}, t) = \partial_t \hat{\mathbf{u}}(\hat{\mathbf{x}}, t)$ , respectively, where and in what follows we denote  $\frac{\partial \phi}{\partial t}$  by  $\partial_t \phi$ . Since the relation  $\mathbf{x}(\hat{\mathbf{x}}, t) = \hat{\mathbf{x}} + \hat{\mathbf{u}}(\hat{\mathbf{x}}, t)$ , the velocity in the current domain with Eulerian coordinates is defined as:  $\mathbf{v}(\mathbf{x}(\hat{\mathbf{x}}, t), t) = \partial_t \mathbf{x} = \partial_t \hat{\mathbf{u}}(\hat{\mathbf{x}}, t) = \hat{\mathbf{v}}(\hat{\mathbf{x}}, t)$ . For the simplicity of notation, we use  $\nabla$  and  $\hat{\nabla}$  to respectively denote  $\nabla_{\mathbf{x}}$  and  $\nabla_{\hat{\mathbf{x}}}$ , which are the gradients with respect to  $\mathbf{x}$  and  $\hat{\mathbf{x}}$ , respectively.

### 2.1. Blood fluid motion

The blood fluid flow is described by the following incompressible Navier-Stokes equations in terms of the velocity  $\mathbf{v}_f$  and the pressure  $p_f$ :

$$\rho_f(\partial_t \mathbf{v}_f + \mathbf{v}_f \cdot \nabla \mathbf{v}_f) - \nabla \cdot \boldsymbol{\sigma}_f = \mathbf{f}_f \text{ in } \Omega_f^t \times (0, T], \quad (1)$$

$$\nabla \cdot \mathbf{v}_f = 0 \text{ in } \Omega_f^t \times (0, T], \quad (2)$$

where  $\rho_f$  is the density of the blood,  $\mathbf{f}_f$  is the body force, and  $\boldsymbol{\sigma}_f$  is the stress rate tensor defined as

$$\boldsymbol{\sigma}_f = -p_f \mathbf{I} + 2\nu_f \rho_f \mathbf{D}(\mathbf{v}_f), \quad (3)$$

here  $\nu_f$  denotes the kinematic viscosity in contrast to the dynamic viscosity  $\mu_f = \nu_f \rho_f$ , and  $\mathbf{D}(\mathbf{v}_f) = \frac{1}{2}(\nabla \mathbf{v}_f + (\nabla \mathbf{v}_f)^T)$  is the strain rate tensor.

### 2.2. Hyperelastic structure motion of the arterial wall

Biological tissues are usually modeled as incompressible. In fact, they undergo very small volume changes under large hydrostatic pressure. Experiments show that during traction, the interstitial water (water is a large component of soft tissues) is squeezed out by collagenous membranes, but then it is reabsorbed when the load is removed. So it stays local and is not removed. In addition, the water is not carrying any traction load, so it is not really part of the mechanical tissue volume. For these reasons, soft biological tissues can be modeled as incompressible. Therefore, the hypothesis of incompressible hyperelastic material is very important in applications [41]. In particular, the arterial wall can be classified mechanically as a solid-fluid mixture [42]: the solid part consists of elastin, collagen, and SMCs [43] while the stress-induced movement of the fluid in and out of the arterial wall can be neglected [42]. Hence, the arterial wall is considered as a homogenized solid, which is sufficiently accurate for most experimental and theoretical studies of the stress distribution in the arterial wall. Under these conditions, arteries behave as incompressible solids at physiological loads [44,45]. In our hemodynamic FSI model, the arterial wall is modeled by a hyperelastic equation in terms of the displacement  $\hat{\mathbf{u}}_s$ . Specifically, it is incompressible, homogeneous, and isotropic with an energy density function  $W$  defined as [46–48]

$$W = \beta_1(\mathbf{I}_B - 3) + \beta_2(\mathbf{I}_B - 3)^2,$$

where  $\beta_1$  and  $\beta_2$  denote the elastic parameters,  $\mathbf{I}_B = \text{tr}(\mathbf{B})$  is the first invariant of the left Cauchy-Green tensor  $\mathbf{B} = \mathbf{F}\mathbf{F}^T$ , and  $\mathbf{F} = \nabla_{\hat{\mathbf{x}}} \mathbf{x} = \mathbf{I} + \nabla_{\hat{\mathbf{x}}} \hat{\mathbf{u}}_s$  denotes the deformation gradient tensor,  $J = \det(\mathbf{F})$ . In order to satisfy the incompressibility condition, the constraint  $J = 1$  with the Lagrangian multiplier  $\hat{p}_s$ , which can be identified as the hydrostatic pressure, is added to the energy density function [41, Eq. (5.85)], leading to

$$\tilde{W} = W - \hat{p}_s(J - 1) = \beta_1(\mathbf{I}_B - 3) + \beta_2(\mathbf{I}_B - 3)^2 - \hat{p}_s(J - 1).$$

Then the first Piola stress,  $\mathbf{P}$ , is described as

$$\mathbf{P} = \frac{\partial \tilde{W}}{\partial \mathbf{F}} = -\hat{p}_s J \mathbf{F}^{-T} + 2 \frac{\partial W}{\partial \mathbf{I}_B} \mathbf{F} = -\hat{p}_s J \mathbf{F}^{-T} + 2(\beta_1 + 2\beta_2(\mathbf{I}_B - 3))\mathbf{F}, \quad (4)$$

where we use the identity  $\frac{\partial J}{\partial \mathbf{F}} = J \mathbf{F}^{-T}$  [41, Eq. (5.87)]. The corresponding Cauchy stress tensor,  $\hat{\sigma}_s$ , is thus defined as

$$\hat{\sigma}_s = J^{-1} \mathbf{P} \mathbf{F}^T = -\hat{p}_s \mathbf{I} + \frac{2}{J} \frac{\partial W}{\partial \mathbf{I}_B} \mathbf{B}.$$

Finally, the incompressible hyperelastic structure equation of the arterial wall in Lagrangian description becomes

$$\hat{\rho}_s \partial_{tt} \hat{\mathbf{u}}_s - \hat{\nabla} \cdot \mathbf{P}(\hat{\mathbf{u}}_s, \hat{p}_s) = \hat{\mathbf{f}}_s, \text{ in } \hat{\Omega}_s \times (0, T], \quad (5)$$

$$J(\hat{\mathbf{u}}_s) = 1, \text{ in } \hat{\Omega}_s \times (0, T]. \quad (6)$$

### 2.3. The biological equation of smooth muscle cells (SMCs)

In this paper, we consider a minimum biological effect that is involved in AAA growth, the smooth muscle cell (SMC) density only, in the biological sub-model. Since the SMC density is decreased dramatically in AAA progression [49], we define the equation of the SMC density,  $S$ , as follows [46]:

$$\partial_t S + \nabla \cdot (\mathbf{v}_s S) - D_S \Delta S = -d_s S, \text{ in } \Omega_s^t \times (0, T], \quad (7)$$

where  $D_S$  denotes the constant diffusion coefficient to model the migration of SMCs in the aneurysm [50],  $\mathbf{v}_s$  is the velocity of the arterial wall defined as  $\mathbf{v}_s = \partial_t \mathbf{u}_s$ ,  $d_s$  is the death rate of SMCs that depends on other biological/chemical concentrations. In this paper, we restrict the biological interaction effect to a minimum by simply assigning a constant value to  $d_s$  in  $\Omega_s^t$  that comprises the aneurysm and its neighbor arterial wall, locally, in addition, we do not intend to develop a detailed and complicated biological interaction model but actually focus on the development of novel numerical methods for solving the presented multiscale FSI problem. Therefore, we just take (7) as a simplified model of the SMC density evolution that holds a slow time scale, together with the attendant FSI problem that holds a fast time scale, we build up our multiscale hemodynamic FSI model to be studied numerically in the rest of this paper.

Since the apoptosis of SMC is a well-known phenomenon in the pathophysiology of AAA that contributes to the loss of elasticity of the arterial wall [51,52], and, both elastic parameters  $\beta_1$  and  $\beta_2$  in (4) play a key role in the formation of the arterial wall's elasticity property, we model  $\beta_1$  and  $\beta_2$  as a function of the SMC density,  $S$  [46]. Although many other cells may account for the elasticity of the arterial wall, such as elastin, extracellular matrix, fibroblast, etc. [53], considering that the reduction of these two elastic parameters directly results in the elasticity loss of the arterial wall which leads to the same effect of the apoptosis of SMC, we thus assume both  $\beta_1$  and  $\beta_2$  are proportional to  $S$  only, for the simplicity [46], that is

$$\beta_i = \beta_{i,0} \frac{S}{S_0}, \quad i = 1, 2, \quad (8)$$

where  $\beta_{i,0}$  are given elastic parameters, and  $S_0$  is the SMC density in health.

Considering that the structure equations of the arterial wall (4)-(6) are defined in Lagrangian description, we can also rewrite the SMCs equation (7) in Lagrangian description as follows

$$J \partial_t \hat{S} + \hat{S} \hat{\nabla} \cdot (J \mathbf{F}^{-1} \hat{\mathbf{v}}_s) - D_S \hat{\nabla} \cdot (J \mathbf{F}^{-1} \mathbf{F}^{-T} \hat{\nabla} \hat{S}) = -d_s J \hat{S}, \text{ in } \hat{\Omega}_s \times (0, T], \quad (9)$$

where we apply the following identities [54]:  $\nabla S = \mathbf{F}^{-T} \hat{\nabla} \hat{S}$  and  $\nabla \cdot \boldsymbol{\psi} = J^{-1} \hat{\nabla} \cdot (J \mathbf{F}^{-1} \hat{\boldsymbol{\psi}})$ . Here  $\hat{\mathbf{v}}_s = \partial_t \hat{\mathbf{u}}_s$  and  $J = \det(\mathbf{I} + \hat{\nabla} \hat{\mathbf{u}}_s)$  through which and the relation (8), the SMCs equation (9) couples with the hyperelastic structure equation (5) and (6) in Lagrangian description.

**Remark 2.1.** We cannot eliminate the structural mass equation (6), namely  $J = 1$ , by directly substituting it into the structural momentum equation (5) because (5) alone cannot guarantee  $J = 1$ , (6) must be enforced as a constraint of (5) that is to be held concurrently through the Lagrange multiplier  $\hat{p}_s$ . On the other hand, (6) means to set up an extra equation with respect to  $\hat{\mathbf{u}}_s$ , that is,  $\det(\mathbf{I} + \hat{\nabla} \hat{\mathbf{u}}_s) = 1$ , which can only be true when  $\hat{\mathbf{u}}_s$  and the Lagrange multiplier  $\hat{p}_s$  satisfy both (5) and (6). Numerically, the discretization of  $J$ ,  $J_h = \det(\mathbf{I} + \hat{\nabla} \hat{\mathbf{u}}_{s,h})$  cannot be guaranteed to equal 1 due to the naturally existing approximation error between  $(\hat{\mathbf{u}}_s, \hat{p}_s)$  and  $(\hat{\mathbf{u}}_{s,h}, \hat{p}_{s,h})$ . Thus we keep  $J$  in the SMCs equation (9) as well, and  $J_h$  in its finite element discretization (26) as shown in Section 4.

### 2.4. Interface conditions

We impose the no-slip interface conditions for the presented hemodynamic FSI system, i.e., both velocity and normal stress are continuous across the interface of the blood fluid and the arterial wall, which can be defined in Eulerian description as follows

$$\mathbf{v}_s = \mathbf{v}_f, \text{ on } \Gamma_I^t \times [0, T], \quad (10)$$

$$\boldsymbol{\sigma}_s \mathbf{n}_s + \boldsymbol{\sigma}_f \mathbf{n}_f = 0, \text{ on } \Gamma_I^t \times [0, T], \quad (11)$$

where  $\mathbf{n}_s, \mathbf{n}_f$  are the outward normal vectors across the interface pointing to the blood fluid side and the arterial wall side, respectively, and  $\mathbf{n}_s = -\mathbf{n}_f$ .

Finally, the entire hemodynamic FSI model is defined by coupling the incompressible Navier-Stokes equations (1)–(3), the hyperelastic incompressible structure equations (4)–(6), and the biological SMCs equation (9) through the interface conditions (10), (11) and the relation (8), and, by combining with appropriately prescribed initial and boundary conditions of the primary unknowns,  $\mathbf{v}_f, \hat{\mathbf{u}}_s$  and  $\hat{S}$ , such as

$$\begin{cases} \mathbf{v}_f(\mathbf{x}, 0) = 0 & \text{in } \Omega_f^t, & \hat{\mathbf{u}}_s(\hat{\mathbf{x}}, 0) = 0 & \text{and } \hat{S}(\hat{\mathbf{x}}, 0) = \hat{S}_0 & \text{in } \hat{\Omega}_s, \\ \mathbf{v}_f = \mathbf{v}_{f,D} & \text{on } \Gamma_{f,D}, & \hat{\mathbf{u}}_s = \hat{\mathbf{u}}_{s,D} & \text{and } \hat{S} = \hat{S}_D & \text{on } \hat{\Gamma}_{s,D}, \\ \boldsymbol{\sigma}_f \mathbf{n}_f = \mathbf{g}_{f,N} & \text{on } \Gamma_{f,N}, & \mathbf{P}_s \hat{\mathbf{n}}_s = \hat{\mathbf{g}}_{s,N} & \text{and } D_S J \mathbf{F}^{-1} \mathbf{F}^{-T} \hat{\nabla} \hat{S} \cdot \hat{\mathbf{n}}_s = \hat{g}_{S,N} & \text{on } \hat{\Gamma}_{s,N}, \end{cases} \quad (12)$$

where  $\mathbf{v}_{f,D}, \hat{\mathbf{u}}_{s,D}$  and  $\hat{S}_D$  are Dirichlet boundary value functions on the Dirichlet boundary part  $\Gamma_{f,D} \subset \Gamma_f^t \setminus \Gamma_I^t$  and  $\hat{\Gamma}_{s,D} \subset \hat{\Gamma}_s \setminus \hat{\Gamma}_I$ , respectively, and,  $\mathbf{g}_{f,N}, \hat{\mathbf{g}}_{s,N}$  and  $\hat{g}_{S,N}$  are Neumann boundary value functions on the Neumann boundary part  $\Gamma_{f,N} = \Gamma_f^t \setminus \Gamma_I^t \setminus \Gamma_{f,D}$  and  $\hat{\Gamma}_{s,N} = \hat{\Gamma}_s \setminus \hat{\Gamma}_I \setminus \hat{\Gamma}_{s,D}$ , respectively, if applicable.

One shall point out that two different time scales are involved in this FSI problem with the aneurysm growth: a fast time scale for the blood fluid-arterial wall interaction, i.e., for (1)–(6) in terms of seconds, while a slow time scale for AAA growth that is significantly related with the SMC density's decay, i.e., for (9) in terms of years. In addition, the moving interface between the blood fluid and the arterial wall,  $\Gamma_I^t$ , keeps moving with time in the same fast time scale to account for the deformable arterial wall that interacts with the blood fluid impact all the time.

### 3. The ALE weak form of FSI involving aneurysms

#### 3.1. Arbitrary Lagrangian–Eulerian mapping

Since the blood fluid equations are defined in the Eulerian domain  $\Omega_f^t$  whereas the hyperelastic structure equations of the arterial wall are defined in the Lagrangian domain  $\hat{\Omega}_s$ , the arbitrary Lagrangian–Eulerian (ALE) mapping is thus introduced to redescribe the fluid domain by adapting to the deformable boundary that is attached to the Lagrangian structure domain, simultaneously, preserving the fixed boundary that is attached to the Eulerian fluid domain. In principle, we define the ALE mapping of the blood fluid domain,  $\mathbf{A} : \hat{\Omega}_f \mapsto \Omega_f^t, \forall t \in (0, T]$  as follows: find  $\mathbf{x}_m \in \Omega_f^t$  such that

$$\mathbf{x}_m = \mathbf{A}(\hat{\mathbf{x}}, t) = \hat{\mathbf{x}} + \mathbf{Ext}(\hat{\mathbf{u}}_s(\hat{\mathbf{x}}, t)|_{\hat{\Gamma}_I}), \quad \forall \hat{\mathbf{x}} \in \hat{\Omega}_f, \quad (13)$$

where  $\mathbf{Ext}(\cdot)$  is an appropriate extension of the structure displacement on the interface  $\hat{\Gamma}_I$ . Clearly, the ALE mapping  $\mathbf{A}$  is a type of time-dependent and bijective affine mapping, and, we always assume  $\mathbf{A} \in W^{2,\infty}(\hat{\Omega}_f^t)^d$  and  $\mathbf{A}^{-1} \in W^{1,\infty}(\Omega_f^t)^d$  [32,55,56]. A classical choice of the extension  $\mathbf{Ext}(\cdot)$  is to consider a harmonic extension operator, i.e., let  $\hat{\mathbf{u}}_m(\hat{\mathbf{x}}, t) = \mathbf{x}_m - \hat{\mathbf{x}} = \mathbf{Ext}(\hat{\mathbf{u}}_s(\hat{\mathbf{x}}, t)|_{\hat{\Gamma}_I})$  that is treated as the displacement of the fluid mesh, satisfying the following Poisson equation

$$\begin{cases} \Delta \hat{\mathbf{u}}_m = 0 & \text{in } \hat{\Omega}_f, \\ \hat{\mathbf{u}}_m = 0 & \text{on } \hat{\Gamma}_f \setminus \hat{\Gamma}_I, \\ \hat{\mathbf{u}}_m = \hat{\mathbf{u}}_s & \text{on } \hat{\Gamma}_I. \end{cases} \quad (14)$$

Thus the moving fluid mesh is obtained by  $\mathbf{x}_m = \hat{\mathbf{x}} + \hat{\mathbf{u}}_m, \forall \hat{\mathbf{x}} \in \hat{\Omega}_f$ . Let  $\mathbf{v}_m$  denote the velocity of the moving fluid mesh, defined as

$$\mathbf{v}_m(\mathbf{x}_m, t) = \partial_t \mathbf{A} \circ \mathbf{A}^{-1}(\mathbf{x}_m) = \partial_t(\hat{\mathbf{x}} + \hat{\mathbf{u}}_m) = \partial_t \hat{\mathbf{u}}_m(\hat{\mathbf{x}}, t). \quad (15)$$

Then we have the material derivative defined on the moving fluid mesh as follows

$$D_t \mathbf{v}_f = \partial_t^{\mathbf{A}} \mathbf{v}_f + (\mathbf{v}_f - \mathbf{v}_m) \cdot \nabla \mathbf{v}_f, \quad (16)$$

where the ALE time derivative  $\partial_t^{\mathbf{A}} \mathbf{v}_f = \partial_t \mathbf{v}_f + \mathbf{v}_m \cdot \nabla \mathbf{v}_f$ . Hence, the momentum equation of the fluid (1) can be reformulated as

$$\rho_f(\partial_t^{\mathbf{A}} \mathbf{v}_f + (\mathbf{v}_f - \mathbf{v}_m) \cdot \nabla \mathbf{v}_f) - \nabla \cdot \boldsymbol{\sigma}_f = \mathbf{f}_f \quad \text{in } \Omega_f^t \times (0, T]. \quad (17)$$

The key reason why the ALE mapping approach works well for FSI problems is because the following Lemma 3.1 holds the so-called  $H^1$ -invariance all the time for any  $\mathbf{v}_f = \mathbf{v}_f(\mathbf{x}(\hat{\mathbf{x}}, t), t)$  and its ALE time derivative  $\partial_t^{\mathbf{A}} \mathbf{v}_f$ , which is the foundation for analyzing the stability and convergence properties of ALE-FEM.

**Lemma 3.1.** [55,56] For any  $t \in (0, T]$ ,  $\mathbf{v}_f(\mathbf{x}, t) \in H^1(\Omega_f^t)^d$  and  $\partial_t^A \mathbf{v}_f(\mathbf{x}, t) \in H^1(\Omega_f^t)^d$  if and only if  $\hat{\mathbf{v}}(\hat{\mathbf{x}}, t) = \mathbf{v}(\mathbf{x}, t) \circ \mathbf{A}(\hat{\mathbf{x}}, t) \in H^1(\hat{\Omega}_f)^d$ .

Lemma 3.1 provides a sufficient and necessary condition for the introduction of the following functional spaces that are adopted for defining the ALE weak form of the presented FSI problem:

$$\begin{aligned}
 \mathbf{V}^f &:= \{\boldsymbol{\psi}_f \in H^1(\Omega_f^t)^d : \boldsymbol{\psi}_f = \hat{\boldsymbol{\psi}}_f \circ \mathbf{A}^{-1}, \hat{\boldsymbol{\psi}}_f \in H^1(\hat{\Omega}_f)^d\}, \\
 \mathbf{V}_0^f &:= \{\boldsymbol{\psi}_f \in \mathbf{V}^f : \boldsymbol{\psi}_f = 0 \text{ on } \Gamma_{f,D}\}, \\
 \mathbf{V}_D^f &:= \{\boldsymbol{\psi}_f \in \mathbf{V}^f : \boldsymbol{\psi}_f = \mathbf{v}_{f,D} \text{ on } \Gamma_{f,D}\}, \\
 \hat{\mathbf{V}}^s &:= \{\hat{\boldsymbol{\psi}}_s \in H^1(\hat{\Omega}_s)^d : \partial_t \hat{\boldsymbol{\psi}}_s = \boldsymbol{\psi}_f \circ \mathbf{A} \text{ on } \hat{\Gamma}_I, \boldsymbol{\psi}_f \in \mathbf{V}^f \cap L^2(\Gamma_I)\}, \\
 \hat{\mathbf{V}}_0^s &:= \{\hat{\boldsymbol{\psi}}_s \in \hat{\mathbf{V}}^s : \hat{\boldsymbol{\psi}}_s = 0 \text{ on } \hat{\Gamma}_{s,D}\}, \\
 \hat{\mathbf{V}}_D^s &:= \{\hat{\boldsymbol{\psi}}_s \in \hat{\mathbf{V}}^s : \hat{\boldsymbol{\psi}}_s = \hat{\mathbf{u}}_{s,D} \text{ on } \hat{\Gamma}_{s,D}\}, \\
 Q^f &:= \{q_f \in L^2(\Omega_f^t) : q_f = \hat{q}_f \circ \mathbf{A}^{-1}, \hat{q}_f \in L^2(\hat{\Omega}_f)\}, \\
 \hat{Q}^s &:= L^2(\hat{\Omega}_s), \\
 \hat{\mathbf{V}}^m &:= H^1(\hat{\Omega}_f)^d, \\
 \hat{\mathbf{V}}_0^m &:= \{\hat{\boldsymbol{\xi}} \in \hat{\mathbf{V}}^m : \hat{\boldsymbol{\xi}} = 0 \text{ on } \hat{\Gamma}_f\}, \\
 \hat{\mathbf{V}}_D^m &:= \{\hat{\boldsymbol{\xi}} \in \hat{\mathbf{V}}^m : \hat{\boldsymbol{\xi}} = 0 \text{ on } \hat{\Gamma}_f \setminus \hat{\Gamma}_I; \hat{\boldsymbol{\xi}} = \hat{\boldsymbol{\psi}}_s \text{ on } \hat{\Gamma}_I, \hat{\boldsymbol{\psi}}_s \in \hat{\mathbf{V}}^s \cap L^2(\hat{\Gamma}_I)\}, \\
 \hat{W}^s &:= H^1(\hat{\Omega}_s), \\
 \hat{W}_0^s &:= \{\hat{w} \in \hat{W}^s : \hat{w} = 0 \text{ on } \hat{\Gamma}_{s,D}\}, \\
 \hat{W}_D^s &:= \{\hat{w} \in \hat{W}^s : \hat{w} = \hat{S}_D \text{ on } \hat{\Gamma}_{s,D}\},
 \end{aligned} \tag{18}$$

where the interface condition (10) is applied to the definition of the space  $\hat{\mathbf{V}}^s$ . Thus, the primary unknowns of our FSI model (1)-(3), (4)-(6), (9) and the harmonic ALE mapping equation (14),  $(\mathbf{v}_f, p_f, \hat{\mathbf{u}}_s, \hat{p}_s, \hat{S}, \hat{\mathbf{u}}_m)$ , belong to  $\mathbf{V}_D^f \times Q^f \times \hat{\mathbf{V}}_D^s \times \hat{Q}^s \times \hat{W}_D^s \times \hat{\mathbf{V}}_D^m$ .

### 3.2. The weak form in the ALE frame

Apply the Piola transformation of surface integrals [54], yields

$$\int_{\Gamma_I^t} \boldsymbol{\sigma}_s \mathbf{n}_s d\mathbf{x} = \int_{\hat{\Gamma}_I} J \hat{\boldsymbol{\sigma}}_s \mathbf{F}^{-T} \hat{\mathbf{n}}_s d\hat{\mathbf{x}} = \int_{\hat{\Gamma}_I} \mathbf{P} \hat{\mathbf{n}}_s d\hat{\mathbf{x}},$$

further utilize the interface condition (11), reads

$$\int_{\Gamma_I^t} \boldsymbol{\sigma}_f \mathbf{n}_f d\mathbf{x} + \int_{\hat{\Gamma}_I} \mathbf{P} \hat{\mathbf{n}}_s d\hat{\mathbf{x}} = 0. \tag{19}$$

Thus in view of (17), we can define the ALE weak form of the presented FSI model (1)-(3), (4)-(6), (9) and (14) as follows: find  $(\mathbf{v}_f, p_f, \hat{\mathbf{u}}_s, \hat{p}_s, \hat{S}, \hat{\mathbf{u}}_m) \in \mathbf{V}_D^f \times Q^f \times \hat{\mathbf{V}}_D^s \times \hat{Q}^s \times \hat{W}_D^s \times \hat{\mathbf{V}}_D^m$  such that

$$\begin{aligned}
 &(\hat{\rho}_s \partial_{tt} \hat{\mathbf{u}}_s, \hat{\boldsymbol{\psi}}_s)_{\hat{\Omega}_s} + (\mathbf{P}(\hat{\mathbf{u}}_s, \hat{p}_s), \nabla \hat{\boldsymbol{\psi}}_s)_{\hat{\Omega}_s} + (J(\hat{\mathbf{u}}_s) - 1, \hat{q}_s)_{\hat{\Omega}_s} + (\rho_f \partial_t^A \mathbf{v}_f, \boldsymbol{\psi}_f)_{\Omega_f^t} \\
 &+ ((\mathbf{v}_f - \partial_t \hat{\mathbf{u}}_m \circ \mathbf{A}^{-1}) \cdot \nabla \mathbf{v}_f, \boldsymbol{\psi}_f)_{\Omega_f^t} + (\boldsymbol{\sigma}_f(\mathbf{v}_f, p_f), \nabla \boldsymbol{\psi}_f)_{\Omega_f^t} + (\nabla \cdot \mathbf{v}_f, q_f)_{\Omega_f^t} = (\hat{\mathbf{f}}_s, \hat{\boldsymbol{\psi}}_s)_{\hat{\Omega}_s} + (\mathbf{f}_f, \boldsymbol{\psi}_f)_{\Omega_f^t},
 \end{aligned} \tag{20}$$

$$(J \partial_t \hat{S}, \hat{w})_{\hat{\Omega}_s} + (\hat{\nabla} \cdot (J \mathbf{F}^{-1} \hat{\mathbf{v}}_s) \hat{S}, \hat{w})_{\hat{\Omega}_s} + (D_S J \mathbf{F}^{-1} \mathbf{F}^{-T} \hat{\nabla} \hat{S}, \hat{\nabla} \hat{w})_{\hat{\Omega}_s} = -(d_S J \hat{S}, \hat{w})_{\hat{\Omega}_s}, \tag{21}$$

$$(\nabla \hat{\mathbf{u}}_m, \nabla \hat{\boldsymbol{\xi}})_{\hat{\Omega}_f} = 0, \tag{22}$$

$$\forall (\boldsymbol{\psi}_f, q_f, \hat{\boldsymbol{\psi}}_s, \hat{q}_s, \hat{\mathbf{w}}, \hat{\boldsymbol{\xi}}) \in \mathbf{V}_0^f \times Q^f \times \hat{\mathbf{V}}_0^s \times \hat{Q}^s \times \hat{\mathbf{W}}_0^s \times \hat{\mathbf{V}}_0^m.$$

#### 4. The finite element approximation in the ALE frame

##### 4.1. The discrete ALE mapping and mixed finite element spaces

To define finite element approximations to (20)–(22), we first triangulate initial domains  $\hat{\Omega}_f$  and  $\hat{\Omega}_s$  with the mesh size  $0 < h < 1$ , and obtain two quasi-uniform triangulations:  $\hat{\mathcal{T}}_{f,h}$  in  $\hat{\Omega}_f$  and  $\hat{\mathcal{T}}_{s,h}$  in  $\hat{\Omega}_s$ , which are conforming through the initial interface  $\hat{\Gamma}_I$ . Then, for any  $t \in (0, T]$ , we numerically solve the ALE mapping (14) by means of the piecewise-linear Lagrangian finite element in the finite element space,  $\hat{\mathbf{V}}_h^m := \{\hat{\boldsymbol{\xi}} \in \hat{\mathbf{V}}^m : \hat{\boldsymbol{\xi}}|_K \in P_1(K)^d, \forall K \in \hat{\mathcal{T}}_{f,h}\}$  where  $P_k$  denotes the  $k$ -th degree piecewise polynomial space, to attain the discrete ALE mapping,  $\mathbf{A}_h$ , which represents the moving fluid mesh, that is, for any  $\hat{\mathbf{x}} \in \hat{\Omega}_f$ , there exists  $\mathbf{x}_m \in \Omega_f^t$  such that

$$\mathbf{x}_m = \mathbf{A}_h(\hat{\mathbf{x}}, t) = \hat{\mathbf{x}} + \hat{\mathbf{u}}_{m,h}, \quad (23)$$

where  $\hat{\mathbf{u}}_{m,h} \in \hat{\mathbf{V}}_{D,h}^m := \{\hat{\boldsymbol{\xi}} \in \hat{\mathbf{V}}_h^m : \hat{\boldsymbol{\xi}} = 0 \text{ on } \hat{\Gamma}_I; \hat{\boldsymbol{\xi}} = \hat{\boldsymbol{\psi}}_s \text{ on } \hat{\Gamma}_I, \hat{\boldsymbol{\psi}}_s \in \hat{\mathbf{V}}_h^s \cap L^2(\hat{\Gamma}_I)\}$ , and  $\hat{\mathbf{V}}_h^s := \{\hat{\boldsymbol{\psi}}_s \in \hat{\mathbf{V}}^s : \hat{\boldsymbol{\psi}}_s|_K \in P_1(K)^d, \forall K \in \hat{\mathcal{T}}_{s,h}\}$ . Thus,  $\mathbf{A}_h$  is smooth and invertible, and, the discrete ALE time derivative is accordingly defined as:  $\partial_t^{\mathbf{A}_h} \boldsymbol{\psi}_f = \partial_t \boldsymbol{\psi}_f + \mathbf{v}_{m,h} \cdot \nabla \boldsymbol{\psi}_f = \partial_t \boldsymbol{\psi}_f + (\partial_t \hat{\mathbf{u}}_{m,h} \circ \mathbf{A}_h^{-1}) \cdot \nabla \boldsymbol{\psi}_f$ .

Let  $\mathcal{T}_{f,h}^t$  be the image of  $\hat{\mathcal{T}}_{f,h}$  under the discrete ALE mapping  $\mathbf{A}_h$ , then  $\mathcal{T}_{f,h}^t = \mathbf{A}_h(\hat{\mathcal{T}}_{f,h}) = \hat{\mathcal{T}}_{f,h} + \hat{\mathbf{u}}_{m,h}$ , based on which we are able to introduce finite element spaces for fluid variables, as:  $\mathbf{V}_h^f := \{\boldsymbol{\psi}_f \in \mathbf{V}^f : \boldsymbol{\psi}_f|_K \in P_1(K)^d, \forall K \in \mathcal{T}_{f,h}^t\}$ ,  $Q_h^f := \{q_f \in Q^f : q_f|_K \in P_1(K), \forall K \in \mathcal{T}_{f,h}^t\}$ . We further introduce the following finite element spaces that are associated with other functional spaces defined in (18):

$$\begin{aligned} \mathbf{V}_{0,h}^f &:= \{\boldsymbol{\psi}_f \in \mathbf{V}_h^f : \boldsymbol{\psi}_f = 0 \text{ on } \Gamma_{f,D}\}, & \mathbf{V}_{D,h}^f &:= \{\boldsymbol{\psi}_f \in \mathbf{V}_h^f : \boldsymbol{\psi}_f = \mathbf{v}_{f,D} \text{ on } \Gamma_{f,D}\}, \\ \hat{\mathbf{V}}_{0,D}^s &:= \{\hat{\boldsymbol{\psi}}_s \in \hat{\mathbf{V}}_h^s : \hat{\boldsymbol{\psi}}_s = 0 \text{ on } \hat{\Gamma}_{s,D}\}, & \hat{\mathbf{V}}_{D,h}^s &:= \{\hat{\boldsymbol{\psi}}_s \in \hat{\mathbf{V}}_h^s : \hat{\boldsymbol{\psi}}_s = \hat{\mathbf{u}}_{s,D} \text{ on } \hat{\Gamma}_{s,D}\}, \\ \hat{Q}_h^s &:= \{\hat{q}_s \in \hat{Q}^s : \hat{q}_s|_K \in P_1(K), \forall K \in \hat{\mathcal{T}}_{s,h}\}, & \hat{\mathbf{V}}_{0,h}^m &:= \{\hat{\boldsymbol{\xi}} \in \hat{\mathbf{V}}_h^m : \hat{\boldsymbol{\xi}} = 0 \text{ on } \hat{\Gamma}_I\}, \\ \hat{\mathbf{W}}_h^s &:= \{\hat{\mathbf{w}} \in \hat{\mathbf{W}}^s : \hat{\mathbf{w}}|_K \in P_1(K), \forall K \in \hat{\mathcal{T}}_{s,h}\}, & \hat{\mathbf{W}}_{0,h}^s &:= \{\hat{\mathbf{w}} \in \hat{\mathbf{W}}_h^s : \hat{\mathbf{w}} = 0 \text{ on } \hat{\Gamma}_{s,D}\}, \\ \hat{\mathbf{W}}_{D,h}^s &:= \{\hat{\mathbf{w}} \in \hat{\mathbf{W}}_h^s : \hat{\mathbf{w}} = \hat{\mathbf{S}}_D \text{ on } \hat{\Gamma}_{s,D}\}. \end{aligned} \quad (24)$$

Here, we employ the equal-order mixed finite element,  $P_1/P_1$  element, with the pressure stabilization scheme [57–60] to approximate the saddle-point problem arising from the FSI equation (20) in the finite element spaces  $(\mathbf{V}_h^f \times \hat{\mathbf{V}}_h^s) \times (Q_h^f \times \hat{Q}_h^s) \subset (\mathbf{V}^f \times \hat{\mathbf{V}}^s) \times (Q^f \times \hat{Q}^s)$ , as shown below in (25).

##### 4.2. Multiscale and monolithic ALE mixed finite element schemes

In this section, we first introduce the semi-discrete mixed finite element approximation to (20)–(22) in the ALE frame, based on which we are then able to define the fully discrete ALE-mixed finite element scheme that can be implemented in numerical algorithms developed in Section 4.3.

Based on the ALE weak form (20)–(22), the semi-discrete ALE-mixed finite element scheme of the presented FSI problem can be defined as follows: find  $(\mathbf{v}_{f,h}, p_{f,h}, \hat{\mathbf{u}}_{s,h}, \hat{p}_{s,h}, \hat{\mathbf{S}}_h, \hat{\mathbf{u}}_{m,h}) \in \mathbf{V}_{D,h}^f \times Q_h^f \times \hat{\mathbf{V}}_{D,h}^s \times \hat{Q}_h^s \times \hat{\mathbf{W}}_{D,h}^s \times \hat{\mathbf{V}}_{D,h}^m$  such that

$$\begin{aligned} &(\hat{\rho}_s \partial_{tt} \hat{\mathbf{u}}_{s,h}, \hat{\boldsymbol{\psi}}_s)_{\hat{\Omega}_s} + (\mathbf{P}(\hat{\mathbf{u}}_{s,h}, \hat{p}_{s,h}), \nabla \hat{\boldsymbol{\psi}}_s)_{\hat{\Omega}_s} + (J_h(\hat{\mathbf{u}}_{s,h}) - 1, \hat{q}_s)_{\hat{\Omega}_s} \\ &+ (\rho_f \partial_t^{\mathbf{A}_h} \mathbf{v}_{f,h}, \boldsymbol{\psi}_f)_{\Omega_f^t} + ((\mathbf{v}_{f,h} - \mathbf{v}_{m,h}) \cdot \nabla \mathbf{v}_{f,h}, \boldsymbol{\psi}_f)_{\Omega_f^t} + (\boldsymbol{\sigma}_f(\mathbf{v}_{f,h}, p_{f,h}), \nabla \boldsymbol{\psi}_f)_{\Omega_f^t} \\ &+ (\nabla \cdot \mathbf{v}_{f,h}, q_f)_{\Omega_f^t} + \alpha_1 \frac{h^2}{\mu_f} (\nabla p_{f,h}, \nabla q_f)_{\Omega_f^t} + \alpha_2 h^2 (\nabla \hat{p}_{s,h}, \nabla \hat{q}_s)_{\hat{\Omega}_s} \\ &+ \sum_{K \in \mathcal{T}_{f,h}^t} \frac{\delta_{SUPG}(h)}{\|\mathbf{v}_{f,h} - \mathbf{v}_{m,h}\|_{0,K}} (R(\mathbf{v}_{f,h}, \mathbf{v}_{m,h}), (\mathbf{v}_{f,h} - \mathbf{v}_{m,h}) \cdot \nabla \boldsymbol{\psi}_f)_K = (\hat{\mathbf{f}}_s, \hat{\boldsymbol{\psi}}_s)_{\hat{\Omega}_s} + (\mathbf{f}_f, \boldsymbol{\psi}_f)_{\Omega_f^t}, \end{aligned} \quad (25)$$



$$(J_h(\hat{\mathbf{u}}_{s,h})\partial_t \hat{S}_h, \hat{w})_{\hat{\Omega}_s} + \left( \nabla \cdot \left( (J_h \mathbf{F}_h^{-1})(\hat{\mathbf{u}}_{s,h})\partial_t \hat{\mathbf{u}}_{s,h} \right) \hat{S}_h, \hat{w} \right)_{\hat{\Omega}_s} + \left( D_S(J_h \mathbf{F}_h^{-1} \mathbf{F}_h^{-T})(\hat{\mathbf{u}}_{s,h}) \nabla \hat{S}_h, \nabla \hat{w} \right)_{\hat{\Omega}_s} \\ = -(d_S J_h(\hat{\mathbf{u}}_{s,h}) \hat{S}_h, \hat{w})_{\hat{\Omega}_s}, \quad (26)$$

$$(\nabla \hat{\mathbf{u}}_{m,h}, \nabla \hat{\xi})_{\hat{\Omega}_f} = 0, \quad \forall (\psi_f, q_f, \hat{\psi}_s, \hat{q}_s, \hat{w}, \hat{\xi}) \in \mathbf{V}_{0,h}^f \times Q^f \times \hat{\mathbf{V}}_{0,h}^s \times \hat{Q}^s \times \hat{W}_{0,h}^s \times \hat{\mathbf{V}}_{0,h}^m, \quad (27)$$

where two pressure stabilization terms,  $\alpha_1 \frac{h^2}{\mu_f} (\nabla p_{f,h}, \nabla q_f)_{\Omega_f}$  and  $\alpha_2 h^2 (\nabla \hat{p}_{s,h}, \nabla \hat{q}_s)_{\hat{\Omega}_s}$  are added to (25) to stabilize the equal-order mixed  $P_1/P_1$  element in  $(\mathbf{V}_h^f \times \hat{\mathbf{V}}_h^s) \times (Q_h^f \times \hat{Q}_h^s)$  [57,60], here  $\alpha_1$  and  $\alpha_2$  are two parameters to be tuned in practice. Furthermore, another stabilization term arising from the streamline-upwind/Petrov–Galerkin (SUPG) scheme [61] is introduced to the last term on the left hand side of (25) in order to avoid any numerical instability that might be induced by the dominant convection effect due to a possibly large Reynolds number from the fluid part, where  $R(\mathbf{v}_{f,h}, \mathbf{v}_{m,h}) = \rho_f \partial_t^{\mathbf{A}_h} \mathbf{v}_{f,h} + (\mathbf{v}_{f,h} - \mathbf{v}_{m,h}) \cdot \nabla \mathbf{v}_{f,h}$ ,  $\mathbf{v}_{m,h} = \partial_t \hat{\mathbf{u}}_{m,h} \circ \mathbf{A}_h^{-1}$ , and,  $\delta_{SUPG}(h)$  is an appropriately chosen local parameter depending on the mesh size  $h$ , the Reynolds number and the velocity  $\mathbf{v}_{f,h}$  in each fluid mesh cell  $K$ .

**Remark 4.1.** Note that in (25) we add the pressure stabilization term,  $\alpha_2 h^2 (\nabla \hat{p}_{s,h}, \nabla \hat{q}_s)_{\hat{\Omega}_s}$ , to the structural mass equation, i.e., the incompressibility constraint of the structure,  $J = 1$ , in its finite element discretization form. In fact, if differentiating both sides of  $J = 1$  with respect to time, we can obtain  $\nabla \cdot \mathbf{v}_s = 0$  by using the identity  $\frac{dJ}{dt} = J \nabla \cdot \mathbf{v}_s$ , and vice versa [56]. We know  $\nabla \cdot \mathbf{v}_s = 0$  is the incompressibility constraint of the structure in Eulerian description, or, in nearly Lagrangian description as well under the infinitesimal strain assumption in which  $\mathbf{x} \approx \hat{\mathbf{x}}$ ,  $\Omega_s^t \approx \hat{\Omega}_s$ ,  $\nabla_{\mathbf{x}} \approx \nabla_{\hat{\mathbf{x}}}$ . Thus, two incompressibility constraints,  $J = 1$  and  $\nabla \cdot \mathbf{v}_s = 0$ , are equivalent under the infinitesimal strain assumption, and due to that,  $\nabla \cdot \mathbf{v}_s = 0$  can also be adopted as the mass equation of the incompressible hyperelastic structure in nearly Lagrangian description. As a consequence, the above pressure stabilization term can be naturally added when the equal-order mixed FEM is applied to discretize both the momentum and the mass equations involving the divergence-free form of structural velocity, and, such a stabilization scheme based upon  $\nabla \cdot \mathbf{v}_s = 0$  is validated stable, robust, and accurate in numerical tests as demonstrated in [62]. Similarly, our stabilized mixed FEM for the incompressible structure shown in (25) with the incompressibility constraint  $J = 1$  in purely Lagrangian description (without any assumption) also elucidates an equally good numerical performance (as shown in Section 5). Though, both approaches given in [62] and the above ALE-FEM (25) have no theoretical proofs to support yet, which will deserve an in-depth analysis in the future.

To define the fully discrete ALE mixed finite element approximation to (20)–(22), we first introduce a uniform partition  $0 = t_0 < t_1 < \dots < t_M = T$  with the time-step size  $\Delta t = T/M$ , set  $t^n = n\Delta t$ ,  $\varphi^n = \varphi(\mathbf{x}^n, t^n)$ , and  $\mathbf{A}_{m,n} = \mathbf{A}_h^n \circ (\mathbf{A}_h^m)^{-1}$  for  $m, n = 1, \dots, M$  and  $m \neq n$ . Then, we choose the second order backward differentiation formula (BDF2) to approximate temporal derivatives  $\partial_t \hat{S}_h$  in (26) and  $\partial_t \hat{\mathbf{u}}_{m,h}$  in (25) as follows

$$(\partial_t \hat{S}_h)^n \approx d_t^{\Delta} \hat{S}_h^n = \frac{3\hat{S}_h^n - 4\hat{S}_h^{n-1} + \hat{S}_h^{n-2}}{2\Delta t}, \quad (\partial_t \hat{\mathbf{u}}_{m,h})^j \approx d_t^{\delta} \hat{\mathbf{u}}_{m,h}^j = \frac{3\hat{\mathbf{u}}_{m,h}^j - 4\hat{\mathbf{u}}_{m,h}^{j-1} + \hat{\mathbf{u}}_{m,h}^{j-2}}{2\delta t}, \quad (28)$$

where the variable time step size  $\delta t \ll \Delta t$ . In fact, since the blood fluid-arterial wall interaction process bears a fast time scale in contrast to the slow time scale that the biological process of SMCs density decay endures, we thus assign a macro time step size,  $\Delta t$ , to the temporal difference scheme of the SMCs equation, and a micro time step size,  $\delta t$ , to the temporal difference scheme of fluid, structure and ALE mapping equations, as shown in (28), (29) and (30).

Further, the BDF2 in the ALE frame can be defined below to approximate the discrete ALE time derivative  $\partial_t^{\mathbf{A}_h} \mathbf{v}_{f,h}$  in (25) with the micro time step size  $\delta t$ :

$$(\partial_t^{\mathbf{A}_h} \mathbf{v}_{f,h})^j \approx d_t^{\mathbf{A}_h} \mathbf{v}_{f,h}^j = \frac{3\mathbf{v}_{f,h}^j(\mathbf{x}) - 4\mathbf{v}_{f,h}^{j-1} \circ \mathbf{A}_{j,j-1} + \mathbf{v}_{f,h}^{j-2} \circ \mathbf{A}_{j,j-2}}{2\delta t}. \quad (29)$$

In addition, we apply the Newmark scheme to the temporal discretization of the hyperelastic structure equation which presents the temporal feature of a wave equation, that is, we employ

$$d_{tt}^N \hat{\mathbf{u}}_{s,h}^j = \frac{2(d_t^N \hat{\mathbf{u}}_{s,h}^j - d_t^N \hat{\mathbf{u}}_{s,h}^{j-1})}{\delta t} - d_{tt}^N \hat{\mathbf{u}}_{s,h}^{j-1}, \quad (30) \\ d_t^N \hat{\mathbf{u}}_{s,h}^j = \frac{2(\hat{\mathbf{u}}_{s,h}^j - \hat{\mathbf{u}}_{s,h}^{j-1})}{\delta t} - d_t^N \hat{\mathbf{u}}_{s,h}^{j-1},$$

to approximate  $\partial_{tt} \hat{\mathbf{u}}_{s,h}$  and  $\partial_t \hat{\mathbf{u}}_{s,h}$ , respectively, in (25). Such defined Newmark scheme (30) is unconditionally stable and owns the second order accuracy with respect to the time step size [63].

Hence, we define the following fully discrete multiscale ALE mixed finite element approximation to (20)–(22): find  $(\mathbf{v}_{f,h}^n, p_{f,h}^n, \hat{\mathbf{u}}_{s,h}^n, \hat{p}_{s,h}^n, \hat{S}_h^n, \hat{\mathbf{u}}_{m,h}^n) \in \mathbf{V}_{D,h}^{f,n} \times Q_h^{f,n} \times \hat{\mathbf{V}}_{D,h}^s \times \hat{Q}_h^s \times \hat{W}_{D,h}^s \times \hat{\mathbf{V}}_{D,h}^m$  such that for  $n = 1, 2, \dots, M$



$$\begin{aligned}
& (\hat{\rho}_s d_{tt}^N \hat{\mathbf{u}}_{s,h}^n, \hat{\boldsymbol{\psi}}_s)_{\hat{\Omega}_s} + (\mathbf{P}(\hat{\mathbf{u}}_{s,h}^n, \hat{p}_{s,h}), \nabla \hat{\boldsymbol{\psi}}_s)_{\hat{\Omega}_s} + (J_h^n(\hat{\mathbf{u}}_{s,h}^n) - 1, \hat{q}_s)_{\hat{\Omega}_s} \\
& + (\rho_f d_t^{A_h} \mathbf{v}_{f,h}^n, \boldsymbol{\psi}_f)_{\Omega_f^n} + \left( (\mathbf{v}_{f,h}^n - \mathbf{v}_{m,h}^n) \cdot \nabla \mathbf{v}_{f,h}^n, \boldsymbol{\psi}_f \right)_{\Omega_f^n} + (\boldsymbol{\sigma}_f(\mathbf{v}_{f,h}^n, p_{f,h}^n), \nabla \boldsymbol{\psi}_f)_{\Omega_f^n} \\
& + (\nabla \cdot \mathbf{v}_{f,h}^n, q_f)_{\Omega_f^n} + \alpha_1 \frac{h^2}{\mu_f} (\nabla p_{f,h}^n, \nabla q_f)_{\Omega_f^n} + \alpha_2 h^2 (\nabla \hat{p}_{s,h}^n, \nabla \hat{q}_s)_{\hat{\Omega}_s} \\
& + \sum_{K \in \mathcal{T}_{f,h}^n} \frac{\delta_{SUPG}(h)}{\|\mathbf{v}_{f,h}^n - \mathbf{v}_{m,h}^n\|_{0,K}} \left( R(\mathbf{v}_{f,h}^n, \mathbf{v}_{m,h}^n), (\mathbf{v}_{f,h}^n - \mathbf{v}_{m,h}^n) \cdot \nabla \boldsymbol{\psi}_f \right)_K = (\hat{\mathbf{f}}_s^n, \hat{\boldsymbol{\psi}}_s)_{\hat{\Omega}_s} + (\mathbf{f}_f^n, \boldsymbol{\psi}_f)_{\Omega_f^n}, \quad (31)
\end{aligned}$$

$$\begin{aligned}
& (J_h^n(\hat{\mathbf{u}}_{s,h}^n) d_t^\Delta \hat{\mathbf{S}}_h^n, \hat{\mathbf{w}})_{\hat{\Omega}_s} + \left( \nabla \cdot \left( (J_h^n(\mathbf{F}_h^n)^{-1})(\hat{\mathbf{u}}_{s,h}^n) d_t^N \hat{\mathbf{u}}_{s,h}^n \right) \hat{\mathbf{S}}_h^n, \hat{\mathbf{w}} \right)_{\hat{\Omega}_s} + \left( D_S \left( J_h^n(\mathbf{F}_h^n)^{-1} (\mathbf{F}_h^n)^{-T} \right) (\hat{\mathbf{u}}_{s,h}^n) \nabla \hat{\mathbf{S}}_h^n, \nabla \hat{\mathbf{w}} \right)_{\hat{\Omega}_s} \\
& = -(d_S J_h^n(\hat{\mathbf{u}}_{s,h}^n) \hat{\mathbf{S}}_h^n, \hat{\mathbf{w}})_{\hat{\Omega}_s}, \quad (32)
\end{aligned}$$

$$(\nabla \hat{\mathbf{u}}_{m,h}^n, \nabla \hat{\boldsymbol{\psi}}_f)_{\hat{\Omega}_f} = 0, \quad \forall \left( \boldsymbol{\psi}_f, q_f, \hat{\boldsymbol{\psi}}_s, \hat{q}_s, \hat{\mathbf{w}}, \hat{\boldsymbol{\xi}} \right) \in \mathbf{V}_{0,h}^{f,n} \times Q^{f,n} \times \mathbf{V}_{0,h}^s \times \hat{Q}^s \times \hat{W}_{0,h}^S \times \hat{\mathbf{V}}_{0,h}^m, \quad (33)$$

where  $\mathbf{v}_{m,h}^n = d_t^\delta \hat{\mathbf{u}}_{m,h}^n \circ (\mathbf{A}_h^n)^{-1}$ .

According to an analogous mixed finite element analysis of the ALE-FEM for the standard FSI problem that comprises a saddle-point system to account for the pair of fluid/structure velocities and the fluid pressure [64], and in light of the pressure-stabilized scheme with  $P_1/P_1$  mixed element, one shall have a stable and convergent mixed finite element approximation (25) in  $(\mathbf{V}_h^f \times \hat{\mathbf{V}}_h^s) \times (Q_h^f \times \hat{Q}_h^s)$  [57,59,60]. As for two varied time step sizes, i.e., the macro one  $\Delta t$  and the micro one  $\delta t$ , we will describe how to choose them and how to carry out two different (macro and micro) time marching processes for (31)–(33) by means of some specific multiscale methods illustrated in Section 4.3.

#### 4.3. Multiscale methods and algorithm descriptions

In the presented FSI problem with AAA progression, the blood fluid-hyperelastic arterial wall interaction process and the biological process have different time scales, that is, the dynamics of FSI changes in the unit of second while the SMCs apoptosis evolves in the unit of day or year, largely comprising a multiscale problem in time. In order to handle such a multiscale challenge in a more efficient as well as a relatively accurate fashion, we need to adopt some temporal multiscale methods to determine variable time steps for the full discretization (31)–(33). Two types of multiscale methods, the heterogeneous multiscale method (HMM) [39] and the seamless multiscale method (SMM) [40], are chosen to cooperate with the developed fully discrete mixed ALE-FEM (31)–(33), then to tackle the presented multiscale FSI problem with AAA growth by a variable time-stepping finite element approximation in the ALE frame. Both HMM's and SMM's characteristics and implementation algorithms are described and discussed below.

##### 4.3.1. The heterogeneous multiscale method (HMM)

We employ the HMM by using the same clock for both the FSI process and the biological process under a basic assumption for the HMM, that is, the microscopic process, i.e., the blood fluid-arterial wall interaction process, is in equilibrium with the unchanged local macroscopic state of the system, i.e., the biological process. Based on the fact that each cardiac cycle takes about 0.8 s, we assume the FSI simulation of each cardiac cycle has the same results if the elasticity of arterial wall and the incoming blood fluid velocity are unchanged, which means FSI solutions in different cardiac cycles present the same profile. Thus, we implement the HMM in the following way that is also illustrated in Fig. 1:

1. Solve the biological SMCs sub-model by using the macro time step size  $\Delta t$ ;
2. Solve the FSI model by using the micro time step size  $\delta t$  in one cardiac cycle 0.8 s for up to  $0.8/\delta t$  steps of the micro time march;
3. Take an average of solutions over the micro time marching steps of  $0.8/\delta t$  obtained in Step 2, then propagate to the next macro time step.

For example, we take  $\Delta t = 1$  day for the biological process, and  $\delta t = 0.01$  s for the FSI process. With 0.8 s as one cardiac cycle time period, we assume the simulation of each cardiac cycle delivers the same results if the elasticity of the arterial wall and the incoming blood fluid are unchanged. Thus, given the hyperelastic coefficients  $(\beta_1, \beta_2)$  computed by the density of SMCs at the previous macro time step, we can simulate the FSI model within the time period 0.8 s using  $\delta t = 0.01$  s for 80 time steps, then take an average of 80 solutions, with which we solve the biological SMCs equation using  $\Delta t = 1$  day. Here, we first run “80 micro time steps” for the FSI model and then run only “1 macro time step” for the biological SMCs

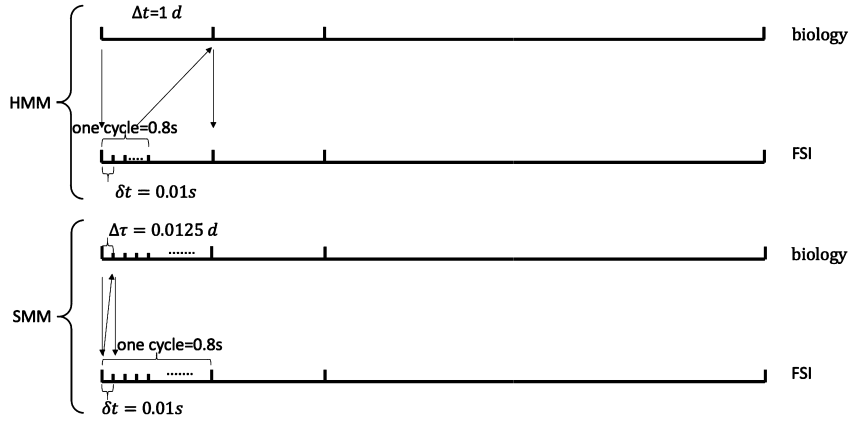


Fig. 1. Illustrations of the HMM vs the SMM.

equation, these two processes are repeated sequentially till the terminal time  $T$  is reached. We describe the implementation algorithm of the HMM in Algorithm 1 below.

---

**Algorithm 1:** The HMM/ALE-FEM for the presented FSI and SMCs models.

---

Sequentially do the following two steps A1 and B1 on the macro time marching for  $m = 1, 2, 3, \dots, M = \lfloor \frac{T}{\Delta t} \rfloor$  with the macro time step  $\Delta t$ .

**A1. The FSI step**

Use the solution of the SMCs equation at the  $(m-1)$ -th macro time step,  $\hat{\mathbf{S}}_h^{m-1}$ , to calculate the elastic parameter  $\beta_1, \beta_2$ . Then do the following micro time marching for  $n = 1, 2, \dots, N = \lfloor \frac{0.8}{\delta t} \rfloor$  with the micro time step  $\delta t$  by conducting the following two-level nonlinear iterations:

- The outer fixed-point iteration with the inner Newton's iteration (with the initial guess  $\hat{\mathbf{v}}_{s,h}^* = \hat{\mathbf{v}}_{s,h}^{n-1}$ ):
  1. Update the fluid mesh: Given  $\hat{\mathbf{u}}_{s,h}^{n-1}$  and  $\hat{\mathbf{v}}_{s,h}^*$ , predict the displacement of the interface by  $\hat{\mathbf{u}}_{s,h}^n = \hat{\mathbf{u}}_{s,h}^{n-1} + \Delta t \cdot \hat{\mathbf{v}}_{s,h}^*$ . Then find  $\hat{\mathbf{u}}_{m,h}^n \in \hat{\mathbf{V}}_{D,h}^m$  with  $\hat{\mathbf{u}}_{m,h}^n|_{\Gamma_f} = \hat{\mathbf{u}}_{s,h}^*|_{\Gamma_f}$  such that

$$(\nabla \hat{\mathbf{u}}_{m,h}^n, \nabla \hat{\mathbf{S}}_{m,h})_{\hat{\Omega}_{f,h}} = 0, \quad \forall \hat{\mathbf{S}}_{m,h} \in \hat{\mathbf{V}}_{0,h}^m.$$

Next, update the fluid mesh by letting  $\mathcal{T}_{f,h}^n := \{\mathbf{x}_m \in \mathbb{R}^d : \mathbf{x}_m = \hat{\mathbf{x}} + \hat{\mathbf{u}}_{m,h}^n, \forall \hat{\mathbf{x}} \in \hat{\mathcal{T}}_{f,h}\}$  and calculate the velocity of the fluid mesh by

$$\mathbf{v}_{m,h}^n = d_t^{\delta} \hat{\mathbf{u}}_{m,h}^n \circ (A_h^n)^{-1}.$$

2. Given  $\mathbf{v}_{f,h}^{n-1}, \mathbf{v}_{f,h}^{n-2}, \hat{\mathbf{v}}_{s,h}^{n-1}, \hat{\mathbf{u}}_{s,h}^{n-1}, \mathbf{v}_{m,h}^n$  and the updated mesh  $\mathcal{T}_{f,h}^n \cup \hat{\mathcal{T}}_{s,h}$ , solve the following FSI system for

$$(\mathbf{v}_{f,h}^n, p_{f,h}^n, \hat{\mathbf{u}}_{s,h}^n, \hat{p}_{s,h}^n) \in \mathbf{V}_{D,h}^{f,n} \times Q_h^{f,n} \times \hat{\mathbf{V}}_{D,h}^s \times \hat{Q}_h^s \text{ such that}$$

$$\begin{aligned} & (\hat{\rho}_s d_{tt}^N \hat{\mathbf{u}}_{s,h}^n, \hat{\boldsymbol{\psi}}_s)_{\hat{\Omega}_s} + (\mathbf{P}(\hat{\mathbf{u}}_{s,h}^n, \hat{p}_{s,h}^n), \nabla \hat{\boldsymbol{\psi}}_s)_{\hat{\Omega}_s} + (J_h^n(\hat{\mathbf{u}}_{s,h}^n) - 1, \hat{q}_s)_{\hat{\Omega}_s} \\ & + (\rho_f d_t^{A_h} \mathbf{v}_{f,h}^n, \boldsymbol{\psi}_f)_{\Omega_f^n} + ((\mathbf{v}_{f,h}^n - \mathbf{v}_{m,h}^n) \cdot \nabla \mathbf{v}_{f,h}^n, \boldsymbol{\psi}_f)_{\Omega_f^n} + (\sigma_f(\mathbf{v}_{f,h}^n, p_{f,h}^n), \nabla \boldsymbol{\psi}_f)_{\Omega_f^n} \\ & + (\nabla \cdot \mathbf{v}_{f,h}^n, q_f)_{\Omega_f^n} + \alpha_1 \frac{h^2}{\mu_f} (\nabla p_{f,h}^n, \nabla q_f)_{\Omega_f^n} + \alpha_2 h^2 (\nabla \hat{p}_{s,h}^n, \nabla \hat{q}_s)_{\hat{\Omega}_s} \\ & + \sum_{K \in \mathcal{T}_{f,h}^n} \frac{\delta_{SUPG}(h)}{\|\mathbf{v}_{f,h}^n - \mathbf{v}_{m,h}^n\|_{0,K}} \left( R(\mathbf{v}_{f,h}^n, \mathbf{v}_{m,h}^n), (\mathbf{v}_{f,h}^n - \mathbf{v}_{m,h}^n) \cdot \nabla \boldsymbol{\psi}_f \right)_K = (\hat{\mathbf{f}}_s^n, \hat{\boldsymbol{\psi}}_s)_{\hat{\Omega}_s} + (\mathbf{f}_f^n, \boldsymbol{\psi}_f)_{\Omega_f^n}, \\ & \forall (\boldsymbol{\psi}_f, q_f, \hat{\boldsymbol{\psi}}_s, \hat{q}_s) \in \mathbf{V}_{0,h}^{f,n} \times Q^{f,n} \times \hat{\mathbf{V}}_{0,h}^s \times \hat{Q}^s, \end{aligned}$$

by means of the Newton's nonlinear iteration until the convergence. Then compute  $\hat{\mathbf{v}}_{s,h}^n = d_t^N \hat{\mathbf{u}}_{s,h}^n$ .

- Check the stopping criterion:  $\|\hat{\mathbf{v}}_{s,h}^* - \hat{\mathbf{v}}_{s,h}^n\|_{0,\hat{\Omega}_s} \leq \text{tolerance}$ . If true, then check  $n+1 > N$ : if yes, then move to the macro time step shown in **B1: The SMCs step**; if not, then move to the next micro time step  $n+1$ . Otherwise, let  $\hat{\mathbf{v}}_{s,h}^* = (\hat{\mathbf{v}}_{s,h}^{n-1} + \hat{\mathbf{v}}_{s,h}^n)/2$  and go back to repeat the above nonlinear iteration steps 1 and 2.

**B1. The SMCs step**

Let  $\hat{\mathbf{u}}_{s,h}^m = \frac{1}{N} \sum_{n=1}^N \hat{\mathbf{u}}_{s,h}^n$  and  $\hat{\mathbf{v}}_{s,h}^m = \frac{1}{N} \sum_{n=1}^N \hat{\mathbf{v}}_{s,h}^n$ . Given  $\hat{\mathbf{S}}_h^{m-1}$  and  $\hat{\mathbf{S}}_h^{m-2}$ , find  $\hat{\mathbf{S}}_h^m \in \hat{\mathbf{W}}_{D,h}^s$  such that

$$\begin{cases} (J_h^m(\hat{\mathbf{u}}_{s,h}^m) d_t^{\Delta} \hat{\mathbf{S}}_h^m, \hat{\mathbf{w}})_{\hat{\Omega}_s} + \left( \nabla \cdot ((J_h^m(\mathbf{F}_h^m)^{-1})(\hat{\mathbf{u}}_{s,h}^m) \hat{\mathbf{v}}_{s,h}^m) \hat{\mathbf{S}}_h^m, \hat{\mathbf{w}} \right)_{\hat{\Omega}_s} + \left( D_s \left( J_h^m(\mathbf{F}_h^m)^{-1}(\mathbf{F}_h^m)^{-1} \right) (\hat{\mathbf{u}}_{s,h}^m) \nabla \hat{\mathbf{S}}_h^m, \nabla \hat{\mathbf{w}} \right)_{\hat{\Omega}_s} \\ = -(d_s J_h^m(\hat{\mathbf{u}}_{s,h}^m) \hat{\mathbf{S}}_h^m, \hat{\mathbf{w}})_{\hat{\Omega}_s}, \quad \forall \hat{\mathbf{w}} \in \hat{\mathbf{W}}_{0,h}^s, \end{cases}$$

where  $\mathbf{F}_h^m = \mathbf{I} + \hat{\nabla} \hat{\mathbf{u}}_{s,h}^m$  and  $J_h^m = \det(\mathbf{F}_h^m)$ .

---

Note that in the SMCs step of Algorithm 1, we take an average of the velocity and the displacement of the arterial wall over  $N$  micro time marching steps. This is just one choice, another choice is that  $\hat{\mathbf{u}}_{s,h}^m$  and  $\hat{\mathbf{v}}_{s,h}^m$  are randomly chosen from the Gaussian distributions computed based on  $N$  sample points  $\{\hat{\mathbf{u}}_{s,h}^n\}_{1 \leq n \leq N}$  and  $\{\hat{\mathbf{v}}_{s,h}^n\}_{1 \leq n \leq N}$ , respectively, which is called the HMM with random variables.

#### 4.3.2. The Seamless multiscale method (SMM)

The SMM uses different clocks for both the FSI process and the biological process under an assumption that the microscopic process can quickly reach its (quasi) “steady-state” status, i.e., a stable and identical solution profile, within each cardiac cycle in contrast to the much slower macroscopic process. Precisely, for our presented FSI model involving the aneurysm growth, the FSI process in which the hyperelastic structure equation is constrained by the SMCs density at every macro time step with the macro time step size  $\Delta t$ , can be relaxed to a (quasi) steady-state in a microscopic time scale with the micro time step size  $\delta t$ , say, after  $k$  micro time steps, where  $k\delta t \ll \Delta t$  and involves multiple cardiac cycles, exactly. Then, we assign  $\Delta\tau = \Delta t/k$  as the new macro time step size. With this new and smaller macro time step size  $\Delta\tau$  and the original micro time step size  $\delta t$ , we only need to conduct one step micro time marching within one step macro time marching. The basic procedure of the SMM is given below that is also illustrated in Fig. 1:

1. Solve the biological SMCs sub-model with the new macro time step size  $\Delta\tau$  for one step, simultaneously, solve the FSI model with the micro time step size  $\delta t$  for one step.
2. Exchange data between the micro and the macro process after each macro and micro time step.

For example, given the hyperelastic coefficients computed by the density of SMCs at the previous macro time step, we can simulate the FSI model with  $\delta t = 0.01$  s. Then by using the obtained numerical solutions of the FSI model, we solve the biological SMCs equation with  $\Delta\tau = 0.0125$  day. When the FSI model is simulated for 80 steps in one cardiac period

---

#### Algorithm 2: The SMM/ALE-FEM of the presented FSI and SMCs models.

---

Sequentially do the following two steps A2 and B2 on the macro time marching for  $m = 1, 2, 3, \dots, \lfloor \frac{T}{\Delta\tau} \rfloor$  with the macro time step  $\Delta\tau$ .

##### A2. The FSI step

Use the solution of SMCs equation at the  $(m-1)$ -th macro time step,  $\hat{\mathbf{S}}^{m-1}$ , to calculate the elastic parameter  $\beta_1, \beta_2$ . Then conduct the following two-level nonlinear iterations with the micro time step  $\delta t$ :

- The outer fixed-point iteration with the inner Newton's iteration (with the initial guess  $\hat{\mathbf{v}}_{s,h}^* = \hat{\mathbf{v}}_{s,h}^{m-1}$ ):

1. Update the fluid mesh: Given  $\hat{\mathbf{u}}_{s,h}^{m-1}$  and  $\hat{\mathbf{v}}_{s,h}^*$ , predict the displacement of the interface by  $\hat{\mathbf{u}}_{s,h}^* = \hat{\mathbf{u}}_{s,h}^{m-1} + \delta t \cdot \hat{\mathbf{v}}_{s,h}^*$ . Then find  $\hat{\mathbf{u}}_{m,h}^m \in \hat{\mathbf{V}}_{D,h}^m$  with  $\hat{\mathbf{u}}_{m,h}^m|_{\Gamma_f} = \hat{\mathbf{u}}_{s,h}^*|_{\Gamma_f}$  such that

$$(\nabla \hat{\mathbf{u}}_{m,h}^m, \nabla \hat{\boldsymbol{\xi}}_{m,h})_{\hat{\Omega}_{f,h}} = 0, \quad \forall \hat{\boldsymbol{\xi}}_{m,h} \in \hat{\mathbf{V}}_{0,h}^m.$$

Next, update the fluid mesh by  $\mathcal{T}_{f,h}^m := \{\mathbf{x}_m \in \mathbb{R}^d : \mathbf{x}_m = \hat{\mathbf{x}} + \hat{\mathbf{u}}_{m,h}^m, \forall \hat{\mathbf{x}} \in \hat{\mathcal{T}}_{f,h}\}$  and calculate the velocity of the fluid mesh by  $\mathbf{v}_{m,h}^m = d_t^\delta \hat{\mathbf{u}}_{m,h}^m \circ (\mathbf{A}_h^m)^{-1}$ .

2. Given  $\mathbf{v}_{f,h}^{m-1}, \mathbf{v}_{f,h}^{m-2}, \hat{\mathbf{v}}_{s,h}^{m-1}, \hat{\mathbf{u}}_{s,h}^{m-1}, \mathbf{v}_{m,h}^m$  and the updated mesh  $\mathcal{T}_{f,h}^m \cup \hat{\mathcal{T}}_{s,h}$ , solve the following FSI system for

$$(\mathbf{v}_{f,h}^m, p_{f,h}^m, \hat{\mathbf{u}}_{s,h}^m, \hat{p}_{s,h}^m) \in \mathbf{V}_{D,h}^{f,m} \times Q_h^{f,m} \times \hat{\mathbf{V}}_{D,h}^s \times \hat{Q}_h^s \text{ such that}$$

$$\begin{aligned} & (\rho_s d_{tt}^N \hat{\mathbf{u}}_{s,h}^m, \hat{\boldsymbol{\psi}}_s)_{\hat{\Omega}_s} + (\mathbf{P}(\hat{\mathbf{u}}_{s,h}^m, \hat{p}_{s,h}^m), \nabla \hat{\boldsymbol{\psi}}_s)_{\hat{\Omega}_s} + (J_h^m(\hat{\mathbf{u}}_{s,h}^m) - 1, \hat{q}_s)_{\hat{\Omega}_s} \\ & + (\rho_f d_t^{\mathbf{A}_h} \mathbf{v}_{f,h}^m, \boldsymbol{\psi}_f)_{\Omega_f^m} + ((\mathbf{v}_{f,h}^m - \mathbf{v}_{m,h}^m) \cdot \nabla \mathbf{v}_{f,h}^m, \boldsymbol{\psi}_f)_{\Omega_f^m} + (\sigma_f(\mathbf{v}_{f,h}^m, p_{f,h}^m), \nabla \boldsymbol{\psi}_f)_{\Omega_f^m} \\ & + (\nabla \cdot \mathbf{v}_{f,h}^m, q_f)_{\Omega_f^m} + \alpha_1 \frac{h^2}{\mu_f} (\nabla p_{f,h}^m, \nabla q_f)_{\Omega_f^m} + \alpha_2 h^2 (\nabla \hat{p}_{s,h}^m, \nabla \hat{q}_s)_{\hat{\Omega}_s} \\ & + \sum_{K \in \mathcal{T}_{f,h}^m} \frac{\delta SUPG(h)}{\|\mathbf{v}_{f,h}^m - \mathbf{v}_{m,h}^m\|_{0,K}} \left( R(\mathbf{v}_{f,h}^m, \mathbf{v}_{m,h}^m), (\mathbf{v}_{f,h}^m - \mathbf{v}_{m,h}^m) \cdot \nabla \boldsymbol{\psi}_f \right)_K = (\hat{\mathbf{f}}_s^m, \hat{\boldsymbol{\psi}}_s)_{\hat{\Omega}_s} + (\mathbf{f}_f^m, \boldsymbol{\psi}_f)_{\Omega_f^m}, \\ & \forall (\boldsymbol{\psi}_f, q_f, \hat{\boldsymbol{\psi}}_s, \hat{q}_s) \in \mathbf{V}_{0,h}^{f,m} \times Q^{f,m} \times \hat{\mathbf{V}}_{0,h}^s \times \hat{Q}^s, \end{aligned}$$

by means of the Newton's nonlinear iteration until the convergence. Then compute  $\hat{\mathbf{v}}_{s,h}^m = d_t^N \hat{\mathbf{u}}_{s,h}^m$ .

- Check the stopping criterion:  $\|\hat{\mathbf{v}}_{s,h}^* - \hat{\mathbf{v}}_{s,h}^m\|_{0,\hat{\Omega}_s} \leq \text{tolerance}$ . If true, then move to the macro time step shown in **B2: The SMCs step**. Otherwise, let  $\hat{\mathbf{v}}_{s,h}^* = (\hat{\mathbf{v}}_{s,h}^{m-1} + \hat{\mathbf{v}}_{s,h}^m)/2$  and go back to repeat the above nonlinear iteration steps 1 and 2.

##### B2. The SMCs step

Given  $\hat{\mathbf{u}}_{s,h}^m$  and  $\hat{\mathbf{v}}_{s,h}^m$  from the  $m$ -th FSI step,  $\hat{\mathbf{S}}_h^{m-1}$  and  $\hat{\mathbf{S}}_h^{m-2}$ , find  $\hat{\mathbf{S}}_h^m \in \hat{W}_{D,h}^S$  such that

$$\begin{cases} (J_h^m(\hat{\mathbf{u}}_{s,h}^m) d_\tau^\Delta \hat{\mathbf{S}}_h^m, \hat{\mathbf{w}})_{\hat{\Omega}_s} + \left( \nabla \cdot ((J_h^m(\mathbf{F}_h^m)^{-1})(\hat{\mathbf{u}}_{s,h}^m) \hat{\mathbf{v}}_{s,h}^m) \hat{\mathbf{S}}_h^m, \hat{\mathbf{w}} \right)_{\hat{\Omega}_s} + \left( D_s \left( J_h^m(\mathbf{F}_h^m)^{-1} (\mathbf{F}_h^m)^{-1} \right) (\hat{\mathbf{u}}_{s,h}^m) \nabla \hat{\mathbf{S}}_h^m, \nabla \hat{\mathbf{w}} \right)_{\hat{\Omega}_s} \\ = -(d_S J_h^m(\hat{\mathbf{u}}_{s,h}^m) \hat{\mathbf{S}}_h^m, \hat{\mathbf{w}})_{\hat{\Omega}_s}, \quad \forall \hat{\mathbf{w}} \in \hat{W}_{0,h}^S, \end{cases}$$

where  $\mathbf{F}_h^m = \mathbf{I} + \hat{\nabla} \hat{\mathbf{u}}_{s,h}^m$  and  $J_h^m = \det(\mathbf{F}_h^m)$ .

---

0.8 s, the biological SMCs equation is also solved for 80 times, i.e.,  $80 \times 0.0125 = 1$  day. Thus, within one day we simulate 80 steps for both the FSI model and the biological SMCs equation. Here, we sequentially run “1 micro time step” for the FSI model and then run “1 macro time step” for the biological SMCs equation, these two processes are repeated sequentially till the terminal time  $T$  is reached. We describe the implementation algorithm of the SMM in Algorithm 2 as follows.

**Remark 4.2.** The SMM exchanges data at every micro time step so that the elasticity of arterial wall changes at every micro time step. Thus it is necessary to make sure the macro time step size  $\Delta\tau$  is relatively small, because a big  $\Delta\tau$  will induce a large change of the elasticity of arterial wall, which might make the microscopic FSI process unstable, to a large extent. On the contrary, the HMM is more stable since the arterial wall only changes its elasticity property at every macro step, and the HMM restarts the FSI process once the change happens.

#### 4.4. Computations of the arterial wall thickness and the aneurysm radius

Considering that the entire arterial wall is incompressible and thus its volume is unchanged, we just need to check the thickness change of the arterial wall in order to investigate the status of AAA growth. In fact, if the thickness of the arterial wall decreases with time, then the surface area of the arterial wall shall simultaneously increase for preserving the volume of the arterial wall. Because a growing AAA keeps expanding the blood vessel lumen and thus increasing the surface area of the arterial wall with the near-end and the far-end of the arterial wall fixed, we are then able to validate the desired status of AAA growth by checking the thickness decrease of the arterial wall. However, it is challenging to accurately compute the thickness of the arterial wall that bears a curved and irregular surface, which is even more difficult in the three-dimensional case.

In the following, we propose an efficient algorithm to compute the thickness of the arterial wall in any shape and any dimension by solving the so-called Eikonal equation [65,66] that is defined in the entire domain  $\Omega = \Omega_f^t \cup \Omega_s^t$  as follows

$$\begin{aligned} |\nabla d(\mathbf{x})| &= \frac{1}{f(\mathbf{x})}, & \mathbf{x} \in \Omega, \\ d(\mathbf{x}) &= 0, & \mathbf{x} \in \partial\Omega. \end{aligned} \quad (34)$$

The solution  $d(\mathbf{x})$  is the shortest time needed to travel from the boundary  $\partial\Omega$  to  $\mathbf{x}$  with the speed  $f(\mathbf{x})$ . If we take  $f(\mathbf{x}) = 1$ , then the solution  $d(\mathbf{x})$  is the distance of the point  $\mathbf{x}$  to the boundary  $\partial\Omega$ . Thus, for any point  $\mathbf{x}$  on the interface  $\Gamma_f^t$ ,  $d(\mathbf{x})$  represents the thickness of the arterial wall at the point  $\mathbf{x}$ . In addition, the maximum value of such defined  $d(\mathbf{x})$  over the entire  $\Omega$  can also deliver the outer radius of the aneurysm since it represents the largest distance from the central point of the aneurysm cavity to the boundary  $\partial\Omega$ .

In order to employ the finite element method to solve (34) in a numerically stable fashion, we add a smoothing term to (34) with  $f = 1$ , and obtain the associated “viscous” Eikonal equation given by

$$\begin{aligned} |\nabla d| &= 1 + \alpha_d \Delta d, & \mathbf{x} \in \Omega, \\ d(\mathbf{x}) &= 0, & \mathbf{x} \in \partial\Omega, \end{aligned} \quad (35)$$

where  $\alpha_d$  is a fine tuned parameter. It can be shown that the artificial viscous term  $\alpha_d \Delta d$  acts to smooth out sharp corners in the solution and guarantees that the solution stays smooth in the entire domain  $\Omega$  [67,65]. As  $\alpha_d$  goes to zero, the solution of (35) converges to the solution of (34). Therefore, we can define the finite element approximation to (35) instead, in the finite element space  $D_h := \{d_h \in H^1(\Omega) : d_h|_K \in P_1(K), \forall K \in \mathcal{T}_{f,h}^t \cup \mathcal{T}_{s,h}^t, d_h = 0 \text{ on } \partial\Omega\}$ , as follows: find  $d_h \in D_h$  such that

$$(|\nabla d_h|, v_h)_\Omega + \alpha_d (\nabla d_h, \nabla v_h)_\Omega = (1, v_h)_\Omega, \quad \forall v_h \in D_h, \quad (36)$$

where we take  $\alpha_d = h/25$  in our computation in Section 5, here  $h$  is the mesh size. And again, we employ the Newton's linearization scheme to iteratively solve the nonlinear equation (36), for which we propose a good initial guess,  $d_h^*$ , by solving the following elliptic equation: find  $d_h^* \in D_h$  such that

$$(\nabla d_h^*, \nabla v_h)_\Omega = (1, v_h)_\Omega, \quad \forall v_h \in D_h. \quad (37)$$

Such a choice of the initial guess can make the Newton's iteration process for solving (36) stable, robust and accurate, which is confirmed feasible and efficient in our numerical simulations shown in Section 5.

**Remark 4.3.** Although that one of the purposes of introducing the Eikonal equation (34) is to find out the exact thickness of the arterial wall at each location of the interface  $\Gamma_f^t$  (the inner surface of the arterial wall), we define (34) in the entire domain  $\Omega = \Omega_f^t \cup \Omega_s^t$  instead of in the arterial wall,  $\Omega_s^t$ , only. That is because the boundary condition of (34) can be easily

**Table 1**  
Physical coefficients and computational parameters for Cases 3D (2D).

Parameter	Description	Value in 3D (2D)
$\rho_s$	Structure density	$1.15 \times 10^3 \text{ kg/m}^3$
$\rho_f$	Fluid density	$1.060 \times 10^3 \text{ kg/m}^3$
$\mu_f$	Fluid dynamic viscosity	$3.7 \times 10^{-3} \text{ Pa}\cdot\text{s}$
$D_S$	Diffusion coefficient of SMCs	$8.64 \times 10^{-11} \text{ m}^2/\text{day}$ [68,69]
$d_S$	Death rate of SMC	0.00258/day [68,70,69] (0.0086/day)
$S_0$	SMCs density at health	$6 \times 10^3 \text{ g/m}^3$ [69]
$\beta_{10}, \beta_{20}$	Elasticity constant of healthy arterial walls	$\beta_{10} = 17.3 \times 10^4, \beta_{20} = 188.1 \times 10^4 \text{ (N/m}^2\text{)}$
# cells	Number of mesh elements	15938 (1926)
# DOFs	Number of degree of freedoms	19626 (5420)
$\delta t$	FSI (micro) time step size	0.01 s
$t_{\text{end}}$	The cardiac cycle time	0.8 s
$\Delta t$	Biological (macro) time step size	1 day (HMM)
$\Delta \tau$	Biological (macro) time step size	0.0125 day (SMM)
$T_{\text{end}}$	Total simulation time	1825 days (365 days).

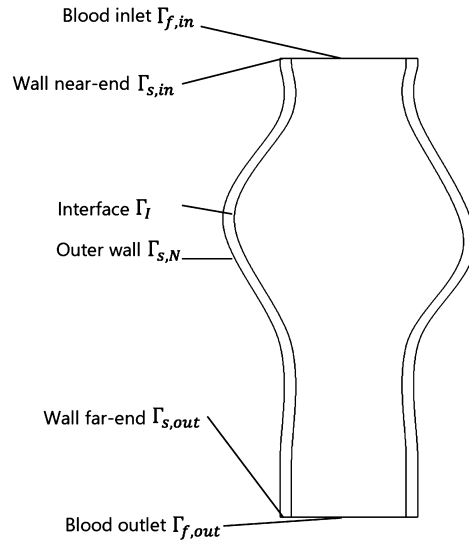


**Fig. 2.** The computational domain of the 2D numerical example.

imposed as a homogeneous Dirichlet boundary condition,  $d(\mathbf{x}) = 0$ , on the outer boundary  $\partial\Omega$  only. Otherwise, if  $\Omega_s^t$  is taken as the domain of (34) instead, then we have to define its boundary condition not only on the outer boundary  $\partial\Omega$  but also on the inner boundary of the arterial wall,  $\Gamma_I^t$ . However, we do not know what the boundary value of  $d(\mathbf{x})$  is on  $\Gamma_I^t$  since it is exactly the thickness of the arterial wall that we solve the Eikonal equation for. Therefore, the Eikonal equation (34) or (35) is defined in the entire domain  $\Omega$ .

## 5. Numerical simulations

In this section, we apply the developed two types of multiscale ALE finite element methods to solve the proposed multiscale hemodynamic FSI problem involving the aneurysm progression. More specifically, we first test two multiscale ALE-FEMs in the two-dimensional case to illustrate some basic ideas about the multiscale FSI simulation with the aneurysm growth. Then, we particularly apply the heterogeneous multiscale ALE-FEM to a three-dimensional example based on a patient CT scan data, and finally compute the thickness of the arterial wall to validate AAA progression. All parameters used in the following numerical simulations are listed in Table 1, where for the parameter that owns different values in cases of 2D and 3D, we show its value in 2D within the parentheses “( )”.

### 5.1. The test of 2D case

We introduce a two-dimensional unsymmetrical domain as showed in Fig. 2. The Dirichlet-type incoming blood flow condition on the inlet  $\Gamma_{f,in}$  for the velocity is prescribed as:  $\mathbf{v}_f|_{\Gamma_{f,in}} = (v_{in}, 0)^T$ , where  $v_{in}$  is defined by the following

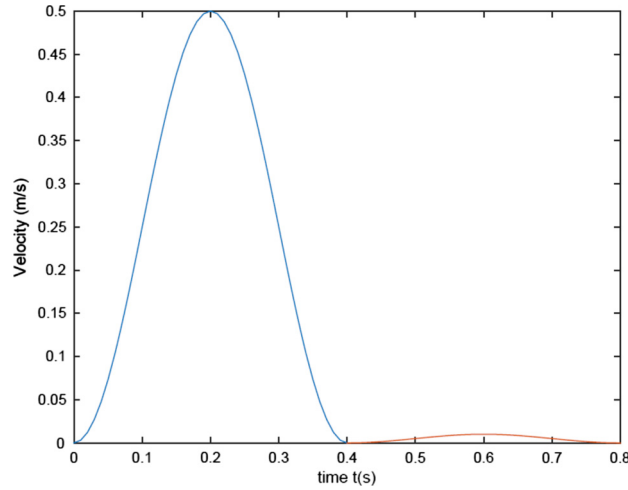


Fig. 3. Profile of the coefficient,  $\tilde{v}_{in}(t)$ , of the horizontal component of the inflow velocity.

function to mimic the incoming blood fluid velocity profile within one cardiac cycle (0.8 s):

$$v_{in}(\mathbf{x}, t) = \tilde{v}_{in}(t)(r^2 - \|\mathbf{x} - \mathbf{x}_0\|^2)/r^2, \text{ where } \tilde{v}_{in}(t) = \begin{cases} 0.5 \left( \sin \left( \frac{2\pi}{0.4}t - \frac{\pi}{2} \right) + 1 \right), & t \in [0, 0.4], \\ 0.01 \left( \sin \left( \frac{2\pi}{0.4}(t - 0.4) - \frac{\pi}{2} \right) + 1 \right), & t \in [0.4, 0.8], \end{cases}$$

where  $\mathbf{x}_0$  is the center of the inlet boundary and  $r$  is the inlet radius. The profile of  $\tilde{v}_{in}(t)$  is shown in Fig. 3. Thus, we define a parabolic inflow on the inlet with a fixed coefficient  $\tilde{v}_{in}$  at each time point  $t$ , whose parabolic shape behaves along with the cardiac cycle. Thus the boundary conditions are describes as

$$\begin{cases} \mathbf{v}_f = \mathbf{v}_f|_{\Gamma_{f,in}} & \text{on } \Gamma_{f,in}, \quad \hat{\mathbf{u}}_s = \mathbf{0} & \text{on } \hat{\Gamma}_{s,in} \cup \hat{\Gamma}_{s,out}, \\ \boldsymbol{\sigma}_f \mathbf{n}_f = \mathbf{0} & \text{on } \Gamma_{f,out}, \quad \mathbf{P}_s \mathbf{n}_s = \mathbf{0} & \text{on } \hat{\Gamma}_{s,N}. \end{cases} \quad (38)$$

For the implementation of the HMM/ALE-FEM, we adopt the same time step size  $\delta t = 0.01$  s for the FSI simulation and  $\Delta t = 1$  day for solving the biological SMCs model, then simulate for 1 year (365 days) so that 365 cardiac cycles are simulated. As for the SMM/ALE-FEM, its time marching process comprises both the FSI and the biological SMCs simulations which run simultaneously, i.e., we run one step of the FSI simulation with  $\delta t = 0.01$  s while we run one step of the biological SMCs simulation with  $\Delta \tau = 0.0125$  day, i.e., we simulate one cardiac cycle (0.8 s) in 1 day ( $= 0.0125 \times 80$ ). However, in order to compare the SMM/ALE-FEM with the HMM/ALE-FEM, we can also simulate the entire system by the SMM/ALE-FEM in 1 year as well which includes 365 cardiac cycles.

For the sake of tracking the growth of AAA as time marches and comparing results from two different multiscale ALE-FEMs, numerical results of the displacement obtained from both the HMM/ALE-FEM and the SMM/ALE-FEM are shown in Figs. 4 and 5, respectively, where the displacement magnitudes are selected when the maximal inflow velocity occurs at  $t = 0.2$  s among one cardiac cycle in one day.

For both methods, FSI model is solved in the time interval  $[0, 0.8]$  on each day, and as examples, we show the results at  $t = 0.2$  on the 1st, 50th, 100th, 150th, 200th, 250th, 300th, 350th day, respectively, noting that in these figures the displacement field of the structure part shows the movement of the arterial wall while the displacement of the fluid part is numerically obtained by  $u_{f,h}^n = u_{f,h}^{n-1} + \delta t \cdot v_{f,h}^n$  with the zero initial displacement. In addition, to show the evolution of the FSI process in one cardiac cycle, we illustrate the magnitude of velocity fields within 0.8 s on the 365th day obtained from the HMM/ALE-FEM in Fig. 6 and from the SMM/ALE-FEM in Fig. 7, as another comparison, where we can see that the arterial wall thus the blood vessel lumen expands during the period of systole (0.1 s - 0.4 s) and contracts during the period of diastole (0.4 s - 0.8 s), corresponding to the prescribed inflow on the inlet behaving as one cardiac cycle.

All corresponding figures of results respectively obtained from the HMM/ALE-FEM and the SMM/ALE-FEM show a quite analogous evolution process in terms of both the displacement and the velocity. Further, to make a quantitative comparison between these two different multiscale ALE-FEMs, we plot and compare the maximum diameter of the aneurysm obtained from the HMM/ALE-FEM with/without random variables and the SMM/ALE-FEM when time marches, as illustrated in Fig. 8, where we see that the variation trend of the maximum diameter along with time presents a slow growth during the first 250 days or so, then starts to grow fast after a transition period of around Day 250 to Day 300, and, such a transition phenomenon is independent of the developed numerical methods. In fact, Fig. 8 indicates that



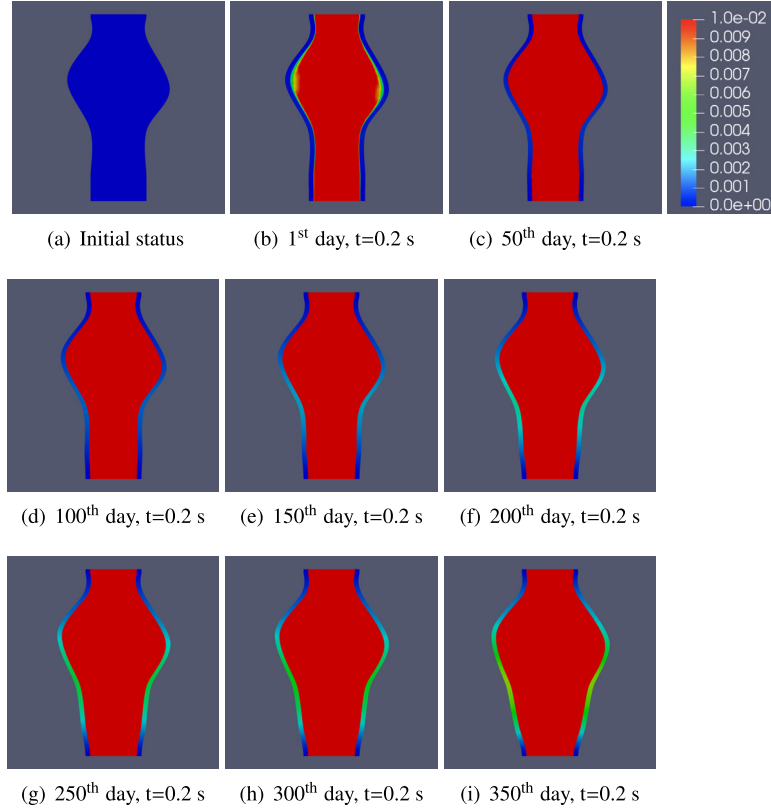


**Fig. 4.** Displacement snapshots for every 50 days by the HMM/ALE-FEM with  $\Delta t = 1$  day and  $\delta t = 0.01$  s. (For interpretation of the colors in the figure(s), the reader is referred to the web version of this article.)

the results from three approaches highly agree with each other in terms of the maximum diameter of the aneurysm. Such coincidence can be explained that the change of elastic parameters in one day is very small in the SMM/ALE-FEM while they keep unchanged in the HMM/ALE-FEM, resulting in a quite similar FSI simulation process for both methods.

Therefore, we only apply the HMM/ALE-FEM to the next 3D example in Section 5.3 for the following reasons:

- It is more reasonable to assume that the elastic parameters are unchanged in one cardiac cycle (0.8 s);
- Two methods generate quite similar results;
- The HMM/ALE-FEM spends less computational cost, relatively.

## 5.2. Convergence test of the HMM/ALE-FEM

To quantitatively validate numerical results of the developed multiscale and monolithic ALE-FEMs, we investigate the convergence property of the HMM/ALE-FEM described in Algorithm 1 as an example. To that end, we conduct the following convergence test for the HMM/ALE-FEM in the 2D case shown in Section 5.1 with the grid doubling. As a whole, we denote the solution of the presented FSI problem as  $(\mathbf{w}, p_f) = ((\mathbf{v}_f, \partial_t \hat{\mathbf{u}}_s), p_f)$ , where  $\mathbf{w} = (\mathbf{v}_f, \partial_t \hat{\mathbf{u}}_s)$  is the velocity variable of FSI, and its numerical solutions of the HMM/ALE-FEM as  $(\mathbf{w}_H, p_{f,H}), (\mathbf{w}_{H/2}, p_{f,H/2}), (\mathbf{w}_{H/4}, p_{f,H/4}), (\mathbf{w}_{H/8}, p_{f,H/8}), (\mathbf{w}_{H/16}, p_{f,H/16})$  on five adjacent mesh levels with the maximum mesh sizes  $H, \frac{H}{2}, \frac{H}{4}, \frac{H}{8}, \frac{H}{16}$ , respectively, from the coarsest level to the finest level, as shown in Table 2 where the concrete value of each mesh size and number of degree of freedoms (DOFs) of the velocity and the pressure over each mesh level are also displayed. Additionally, we choose a time step size that is much smaller than the smallest mesh size  $\frac{H}{16}$ , e.g.,  $\delta t = 0.00001$ , to carry out numerical computations on all mesh levels with the least influence from the time step size over the total approximation accuracy.

Obviously, we do not know the real solution of the presented FSI problem,  $(\mathbf{w}_{real}, p_{f,real})$ , for this 2D example. In order to show a comparable convergence rate of numerical solutions of the HMM/ALE-FEM for both the velocity and the pressure in their energy norms, i.e., the velocity's approximation error in  $H^1$  norm and the pressure's approximation error in  $L^2$  norm, we take numerical solutions of both the velocity and the pressure on the finest mesh level,  $\mathbf{w}_{H/16}$  and  $p_{f,H/16}$ , as their "real" solutions, numerically, i.e.,  $(\mathbf{w}_{real}, p_{f,real}) \approx (\mathbf{w}_{H/16}, p_{f,H/16})$ .

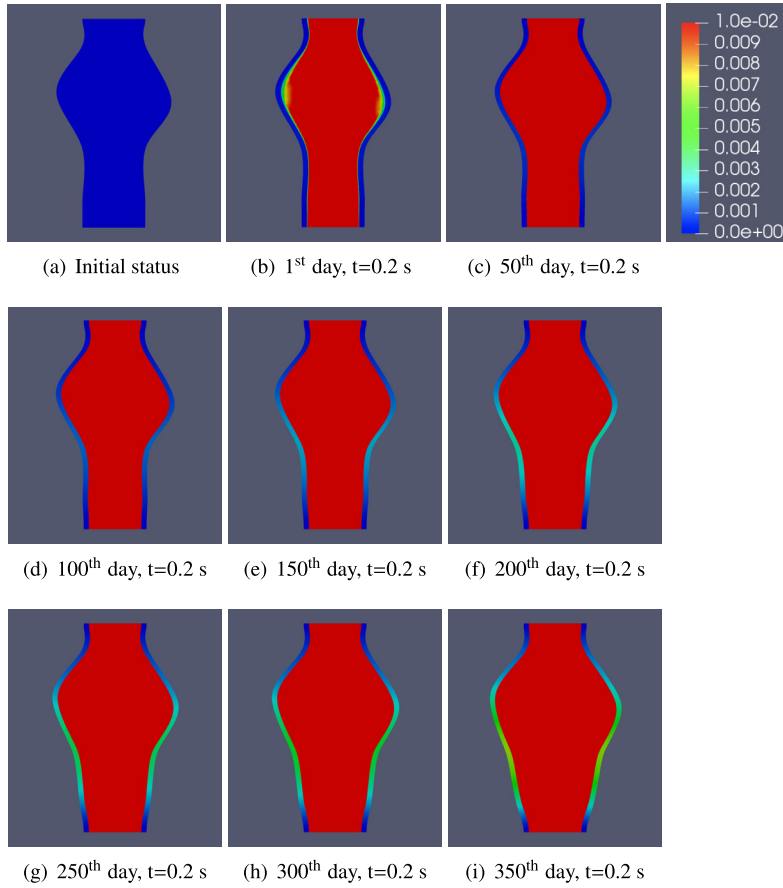


**Fig. 5.** Displacement snapshots for every 50 days by the SMM/ALE-FEM with  $\Delta t = 0.0125$  day and  $\delta t = 0.01$  s.

**Table 2**

Mesh sizes and # of DOFs of velocity ( $\mathbf{w}_h$ ) and pressure ( $p_{f,h}$ ) over five mesh levels.

Mesh size	# of DOFs of $\mathbf{w}_h$	# of DOFs of $p_{f,h}$
$H = 8.2122$	576	196
$\frac{H}{2} = 4.1086$	2168	688
$\frac{H}{4} = 2.0543$	8266	2557
$\frac{H}{8} = 1.0271$	32258	9841
$\frac{H}{16} = 0.5135$	127426	38593

**Table 3**

Convergence results of the HMM/ALE-FEM for the 2D example.

$h$	$H$	$\frac{H}{2}$	$\frac{H}{4}$	$\frac{H}{8}$
$\ \mathbf{w}_{real} - \mathbf{w}_h\ _1$	1.9565	1.0114	0.4876	0.23
Order		0.9520	1.0525	1.0842
$\ p_{f,real} - p_{f,h}\ _0$	0.4884	0.2496	0.0882	0.0399
Order		0.9686	1.4999	1.1440

After carrying out the HMM/ALE-FEM and  $P_1/P_1$  element with the pressure stabilization through Algorithm 1 over the grid doubling for the 2D example, we obtain the convergence results shown in Table 3 and Fig. 9 for both the velocity and the pressure in their energy norms on four coarse mesh levels at  $t = 0.1$ . These numerical results clearly illustrate that the first order convergence rate is obtained for approximation errors of both the velocity and the pressure in their energy norms, i.e.,  $\|\mathbf{w}_{real} - \mathbf{w}_h\|_1 = O(h)$  and  $\|p_{f,real} - p_{f,h}\|_0 = O(h)$ . They further validate the existing theoretical results while the lowest equal-order  $P_1/P_1$  element with the pressure stabilization technique is utilized to discretize the

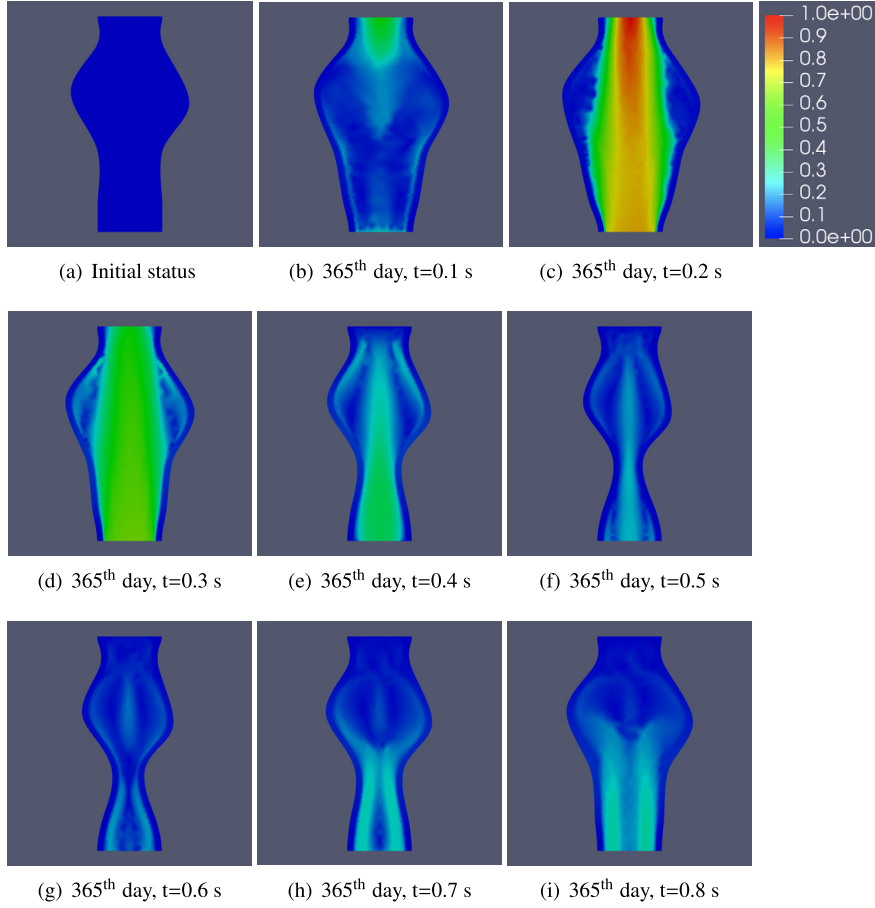


**Fig. 6.** Velocity snapshots in one cardiac cycle for every 0.1 s on the 365th day by the HMM/ALE-FEM.

derived saddle-point system in (31)–(33), that is, considering the regularity properties of both the velocity and the pressure in the presented FSI model, i.e.,  $\mathbf{w} \in H^2(\Omega_f^t) \times H^2(\hat{\Omega}_s)$  and  $p_f \in H^1(\Omega_f^t)$  as a smooth interface  $\Gamma_i^t \in C^2$  [71,55,32], we shall expect the first order optimal convergence rate for both the velocity in  $H^1$  norm and the pressure in  $L^2$  norm [57,59,60]. Therefore, as shown in Table 3 and Fig. 9, the obtained optimal convergence rate for both the velocity and the pressure in their energy norms ensure that our developed HMM/ALE-FEM is accurate and reliable for the presented FSI model.

### 5.3. The 3D validation on a patient CT scan data

In this section, we further validate our developed multiscale and monolithic ALE-FEM methods in the 3D case, where the computational domain, shown in Fig. 11, takes the local aneurysm part from a reconstruction of the full-body CT scan data of a patient, as illustrated in Fig. 10. In order to validate the developed numerical methods on the 3D CT scan data, we compare our numerical results with the clinical patient data on AAA growth reported in [72]. All boundary and initial conditions are the same with the 2D case studied in Section 5.1 except for the initial condition of the SMCs equation. Note that the density of SMCs is correlated to the elasticity of the arterial wall, more specifically, a low density of SMCs yields a large deformation while a high density of SMCs remains the shape of the arterial wall. Therefore, to initially form an aneurysm on the arterial wall with which we can start our 3D multiscale FSI simulation instantly, we artificially define the following initial condition for (9) through the following likelihood of “Gaussian distribution” function, with little information about the location where the maximum diameter of the aneurysm actually occurs during its growth,

$$S = S_0 \left( 1 - \frac{\omega}{\gamma \sqrt{2\pi}} e^{-\frac{1}{2} \left( \frac{z-\mu}{\gamma} \right)^2} \right). \quad (39)$$

This function depends on the  $z$  variable along the normal direction of the outlet surface, as shown in Fig. 12, and,  $\mu$  is the mean of the distribution at which the initial value of the density of SMCs,  $S$ , reaches its minimum. As a consequence,

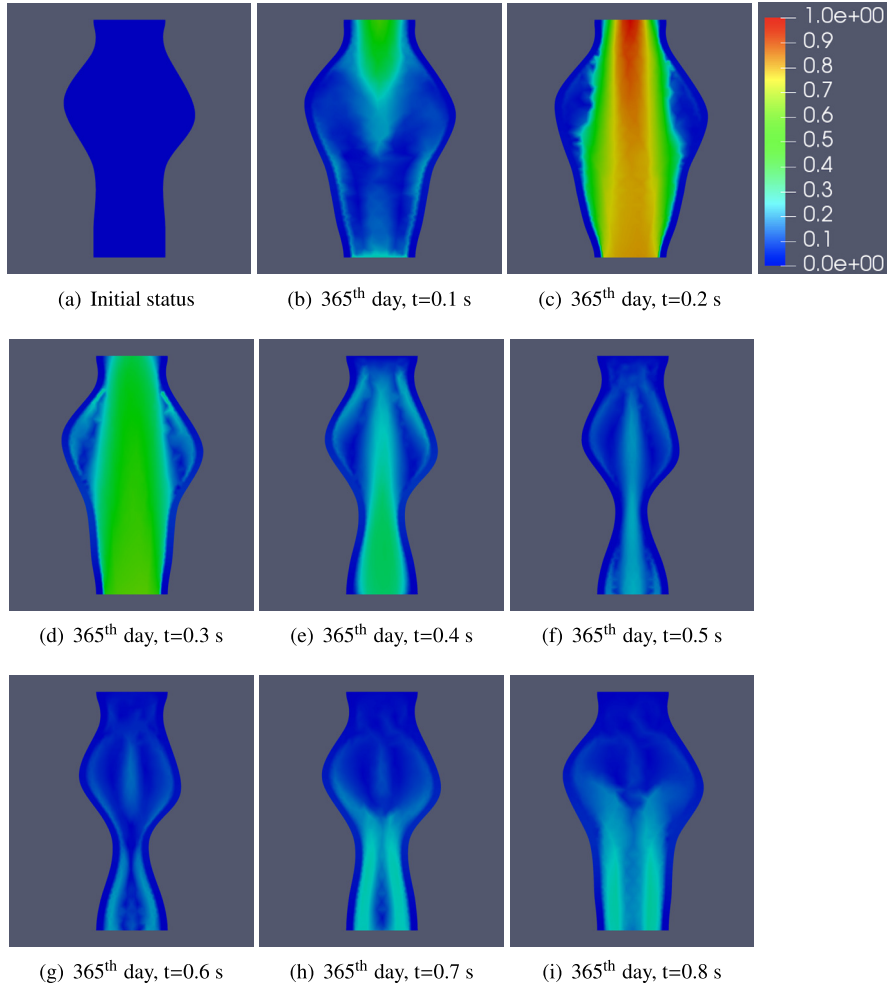


**Fig. 7.** Velocity snapshots in one cardiac cycle for every 0.1 s on the 365th day by the SMM/ALE-FEM.

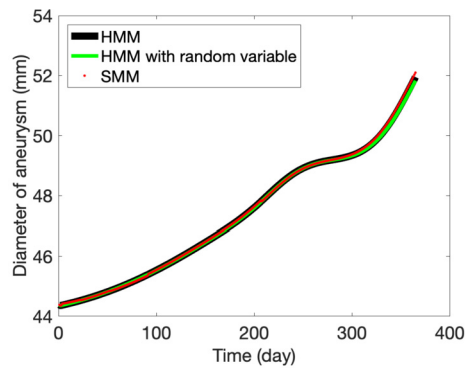


**Fig. 8.** The growth status of the maximum diameter of AAA over 365 days obtained by HMM/ALE-FEM, HMM/ALE-FEM with random variables and SMM/ALE-FEM.

the largest deformation of the arterial wall and thus the maximum diameter of the aneurysm may occur at the same place where  $z = \mu$ . Therefore, (39) actually describes an inverse version of the normal Gaussian distribution function for the initial value of  $S$ , with  $\gamma$  as the standard deviation. In addition,  $\omega$  is a fine-tuned parameter in (39) that controls the drop trend of the initial value of  $S$  near the aneurysm. For example, in our 3D numerical experiment below, we take  $\mu = -0.64$ ,  $\gamma = 0.008$  and thus  $\omega = 0.01$  to assume that the density of SMCs,  $S$ , is initially close to  $\frac{S_0}{2}$  at the mean of the distribution,

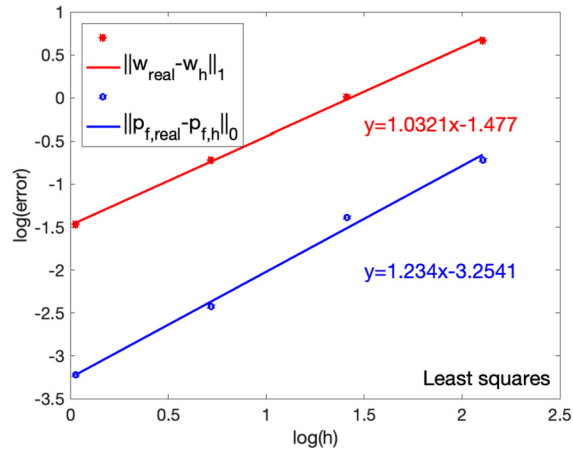


Fig. 9. Convergence trend of the HMM/ALE-FEM for the 2D example.

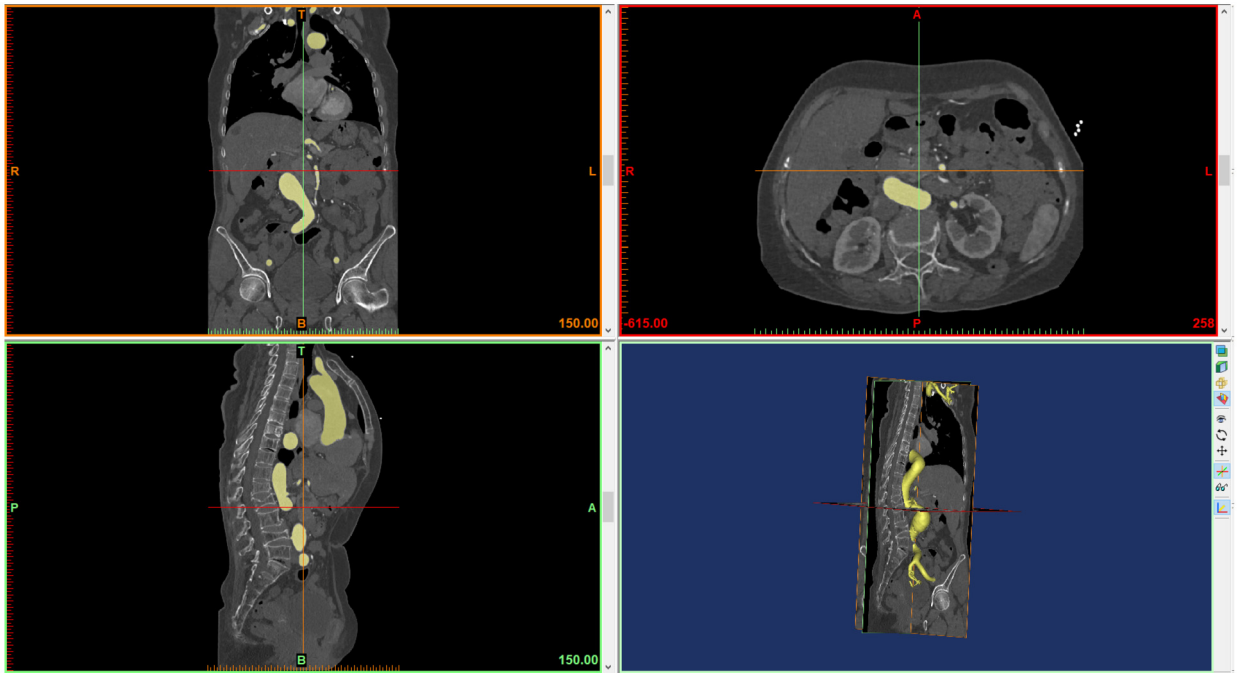
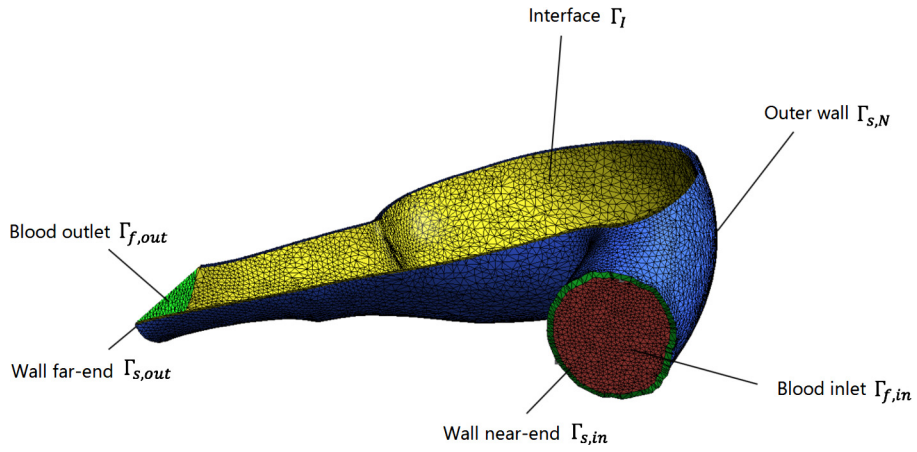


Fig. 10. Different angle of views of a patient's CT scan data.

where the aneurysm likely owns its initial maximum diameter obtained from the reconstruction of a patient's 3D CT scan data, and, will be able to capture its largest size around the same place during AAA growth.

We implement the developed HMM/ALE-FEM for the proposed multiscale FSI model, and simulate the growth of the aneurysm in 5 years and compute 365 heartbeat cycles in each year. Since the maximum velocity of the blood fluid achieves at  $t = 0.2$  s in each cardiac cycle, we take numerical results obtained at  $t = 0.2$  s of the 365th cardiac cycle (on the 365th day) in each year to demonstrate the performance of our FSI simulation in 3D case, such as the displacement results of the arterial wall in each year. Then we simulate our developed model for this patient to predict the growth of AAA in five years, the displacement fields of the arterial wall along the time are shown in Fig. 13. The diameter of the aneurysm grows from 34 mm to 42.5 mm over five years, which clearly shows that the deformation of the aneurysm tends to be larger and larger each year so that it is more significant than other parts of the arterial wall. In other words, the rupture risk has a much higher possibility to occur at the aneurysm that bears the largest deformation, as shown by our numerical results which coincides with the reality.

Moreover, we also compare the prediction of AAA growth (in terms of the maximum diameter of the aneurysm) with the historical data of AAA patients available in [72], as compared in Fig. 14. The historical data of AAA growth are collected



**Fig. 11.** A portion of the 3D numerical example's computational domain.

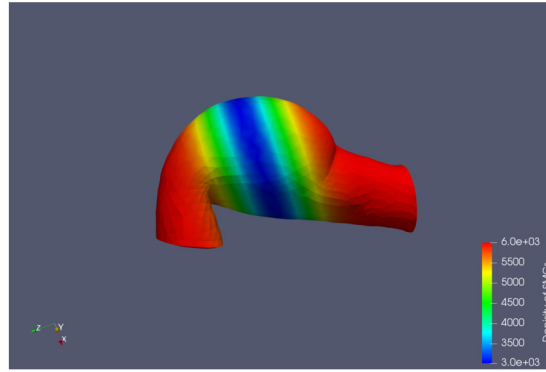


**Fig. 12.** The initial density of SMCs based on an inverse Gaussian distribution.

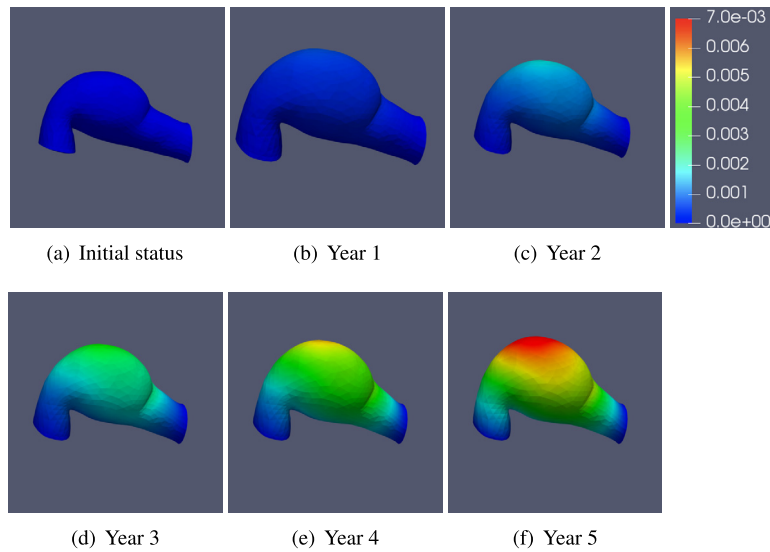


**Fig. 13.** Displacement snapshots in each year over five years.



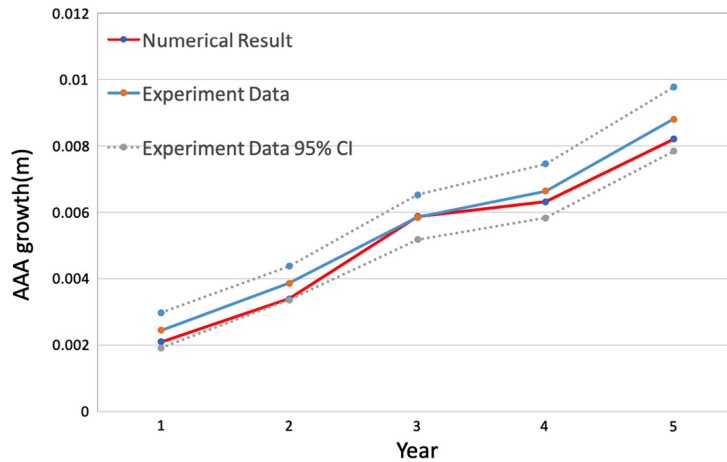


Fig. 14. Comparisons between our numerical results and the experimental data.

among 352 patients followed by a mean of  $55.2 \pm 37.4$  months [72]. The mean growth rate varied from  $2.07 \pm 3.23$  to  $4.72 \pm 5.93$  mm/year for five years. Our predicted result (2 mm/year) lies in the 95% confidence interval of the clinical data reported in [72] and thus is validated by the available clinical data, as illustrated in Fig. 14. In addition, we can also see that a transition phenomenon exists in Fig. 14 between Year 3 and Year 4, which occurs after a slow AAA growth period prior to Year 3, and before a fast AAA growth period starting at Year 4. A similar transition phenomenon of AAA growth status is also observed in the 2D case shown in Fig. 8, which may explain that such a transition phenomenon existing in AAA growth process is independent of the dimension as well, besides that it is independent of numerical methods as shown in Section 5.1. We believe that such a transition process of AAA growth, which gradually transits from a slow growth period to a fast growth period, is essentially determined by the hyperelastic property of the structure model adopted in our study, and, the nonlinear stress-strain relationship owned by the hyperelasticity model (e.g., see [41, Figure 5.3]) shall play a key role behind this since it governs the deformation of the arterial wall as well as the aneurysm growth all the time.

To further evaluate the reliability and feasibility of the developed multiscale ALE-FEM, by means of the presented Eikonal equation (34), we compute and predict the thickness of the arterial wall that is highly related to AAA rupture risk. Our numerical prediction of the arterial wall's thickness shall endure a long-term simulation, say, after eight years, we obtain the numerical result shown in Fig. 15, where the thickness at the aneurysm is decreased by 35% from 1.15 mm to 0.75 mm and has a much higher rupture risk than other parts of the arterial wall. Moreover, numerical results suggest that the decreasing rate of the arterial wall's thickness is more related to AAA rupture risk rather than the absolute thickness itself. For instance, the arterial wall at Point B is thinner than that at Point C, but the deformation at Point B is much less than that at Point C, therefore the rupture risk at Point C is higher, as illustrated in Fig. 15.

## 6. Conclusion

In this numerical study, we develop two types of multiscale and monolithic ALE-finite element methods (ALE-FEM) for the hemodynamic FSI problem that involves the aneurysm progression, and, the designed ALE-finite element approximation algorithms of both heterogeneous multiscale method (HMM) and seamless multiscale method (SMM) can predict the long-term growth of abdominal aortic aneurysms (AAA) very well. In addition to providing all technical aspects of two distinct and efficient numerical approaches, we apply both the HMM/ALE-FEM and the SMM/ALE-FEM to a schematic 2D example with the aneurysm growth, and obtain coincident results. Numerical validation in terms of a convergence test is also provided for the developed HMM/ALE-FEM to illustrate that both velocity and pressure's approximation errors hold optimal convergence properties in  $L^2$  and  $H^1$  norms. Further, we apply the HMM/ALE-FEM to a three-dimensional AAA patient's CT scan imaging data. Our numerical results demonstrate that the prediction lies in a reasonable range based on AAA patients' historical data. Additionally, this numerical approach also provides an estimation of arterial wall thickness which contributes to AAA rupture risk as well.

## CRedit authorship contribution statement

**Wenrui Hao:** Conceptualization, Investigation, Writing – original draft. **Pengtao Sun:** Formal analysis, Methodology, Project administration, Supervision, Writing – review & editing. **Jinchao Xu:** Data curation, Funding acquisition, Resources. **Lian Zhang:** Software, Validation, Visualization.

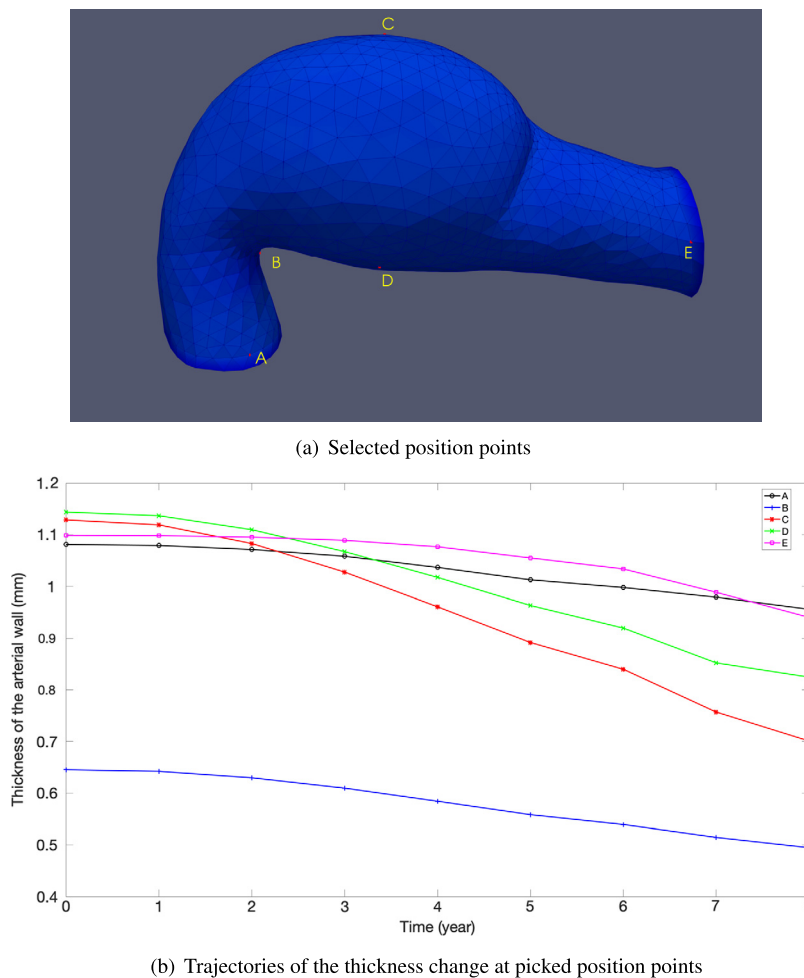


Fig. 15. Dynamics of the arterial wall thickness at five picked position points over 8 years.

## Declaration of competing interest

The authors declare that they have no known competing financial interests or personal relationships that could have appeared to influence the work reported in this paper.

## Acknowledgements

W. Hao was supported in part by AHA grant 17SDG33660722. P. Sun was supported by a grant from The Simons Foundation (MPS-706640, PS). J. Xu was supported in part by Verne M. Willaman Professor Chair Fund. L. Zhang was supported by the Center for Computational Mathematics and Applications (CCMA), Penn State University.

## References

- [1] S. Aggarwal, A. Qamar, V. Sharma, A. Sharma, Abdominal aortic aneurysm: a comprehensive review, *Exp. Clin. Cardiol.* 16 (2011) 11–15.
- [2] D.P. Howard, A. Banerjee, J.F. Fairhead, A. Handa, L.E. Silver, P.M. Rothwell, Population-based study of incidence of acute abdominal aortic aneurysms with projected impact of screening strategy, *J. Am. Heart Assoc.* 4 (2015) e001926.
- [3] F. Collins, H. Varmus, A new initiative on precision medicine, *N. Engl. J. Med.* 372 (2015) 793–795.
- [4] P. Heidenreich, J. Trogdon, O. Khavjou, J. Butler, K. Dracup, M. Ezekowitz, E. Finkelstein, Y. Hong, C. Johnston, A. Khera, Forecasting the future of cardiovascular disease in the United States: a policy statement from the American Heart Association, *Circulation* 123 (2011) 933–944.
- [5] G. Kolata, Genetic heart disease risk eased by healthy habits, study finds, <https://www.nytimes.com/2016/11/14/health/genetic-heart-disease-risk-eased-by-healthy-habits-study-finds.html>, 2016.
- [6] S. Canic, Blood flow through compliant vessels after endovascular repair: wall deformations induced by the discontinuous wall properties, *Comput. Vis. Sci.* 4 (2002) 147–155.
- [7] S. Canic, D. Mirkovic, A hyperbolic system of conservation laws in modeling endovascular treatment of abdominal aortic aneurysm, in: *Hyperbolic Problems: Theory, Numerics, Applications*, Springer, 2001, pp. 227–236.

- [8] S. Canic, K. Ravi-Chandar, Z. Krajcar, D. Mirkovic, S. Lapin, Mathematical model analysis of wallstent and aneurx: dynamic responses of bare-metal endoprosthesis compared with those of stent-graft, *Texas Heart Inst. J.* 32 (2005) 502.
- [9] P. Erhart, A. Hyhlík-Durr, P. Geisbusch, D. Kotelis, M. Müller-Eschner, T.C. Gasser, H. von Tengg-Kobligh, D. Bockler, Finite element analysis in asymptomatic, symptomatic, and ruptured abdominal aortic aneurysms: in search of new rupture risk predictors, *Eur. J. Vasc. Endovasc. Surg.* 49 (2015) 239–245.
- [10] P. Fok, Growth of necrotic cores in atherosclerotic plaque, *Math. Med. Biol.* 29 (2011) 301–327.
- [11] C. Poelma, P.N. Watton, Y. Ventikos, Transitional flow in aneurysms and the computation of haemodynamic parameters, *J. R. Soc. Interface* 12 (2015).
- [12] D. Roy, S. Lerouge, K. Inaekyan, C. Kauffmann, R. Mongrain, G. Soulez, Experimental validation of more realistic computer models for stent-graft repair of abdominal aortic aneurysms, including pre-load assessment, *Int. J. Numer. Methods Biomed. Eng.* 32 (2016).
- [13] E. Soudah, E.Y. Ng, T.H. Loong, M. Bordone, U. Pua, S. Narayanan, CFD modelling of abdominal aortic aneurysm on hemodynamic loads using a realistic geometry with CT, *Comput. Math. Methods Med.* 2013 (2013) 472564.
- [14] J. Tambaa, M. Kosor, S. Canic, Mathematical modeling of vascular stents, *SIAM J. Appl. Math.* 70 (2010) 1922–1952.
- [15] F. Tian, L. Zhu, P. Fok, X. Lu, Simulation of a pulsatile non-Newtonian flow past a stenosed 2d artery with atherosclerosis, *Comput. Biol. Med.* 43 (2013) 1098–1113.
- [16] Q. Wang, A hydrodynamic theory for solutions of nonhomogeneous nematic liquid crystalline polymers of different configurations, *J. Chem. Phys.* 116 (2002) 9120–9136.
- [17] J. Wu, S.C. Shadden, Coupled simulation of hemodynamics and vascular growth and remodeling in a subject-specific geometry, *Ann. Biomed. Eng.* 43 (2015) 1543–1554.
- [18] X. Yang, G. Forest, W. Mullins, Q. Wang, Dynamic defect morphology and hydrodynamics of sheared nematic polymers in two space dimensions, *J. Rheol.* 53 (2009) 589–615.
- [19] Y. Yu, Fluid-structure interaction modeling in 3D cerebral arteries and aneurysms, in: *Biomedical Technology*, Springer, 2018, pp. 123–146.
- [20] Y. Yu, P. Perdikaris, G. Karniadakis, Fractional modeling of viscoelasticity in 3D cerebral arteries and aneurysms, *J. Comput. Phys.* 323 (2016) 219–242.
- [21] J. Zhao, X. Yang, J. Shen, Q. Wang, A decoupled energy stable scheme for a hydrodynamic phase-field model of mixtures of nematic liquid crystals and viscous fluids, *J. Comput. Phys.* 305 (2016) 539–556.
- [22] K. Yang, P. Sun, L. Wang, J. Xu, L. Zhang, Modeling and simulation for fluid-rotating structure interaction, *Comput. Methods Appl. Mech. Eng.* 311 (2016) 788–814.
- [23] A. Barker, X. Cai, Scalable parallel methods for monolithic coupling in fluid-structure interaction with application to blood flow modeling, *J. Comput. Phys.* 229 (2010) 642–659.
- [24] P. Causin, J. Gerbeau, F. Nobile, Added-mass effect in the design of partitioned algorithms for fluid–structure problems, *Comput. Methods Appl. Mech. Eng.* 194 (2005) 4506–4527.
- [25] S. Idelsohn, P. Del, R. Rossi, E.O. nate, Fluid-structure interaction problems with strong added-mass effect, *Int. J. Numer. Methods Eng.* 80 (2009) 1261–1294.
- [26] C. Taylor, T. Hughes, C. Zarins, Finite element modeling of blood flow in arteries, *Comput. Methods Appl. Mech. Eng.* 158 (1998) 155–196.
- [27] R. Torii, M. Oshima, T. Kobayashi, K. Takagi, Numerical simulation system for blood flow in the cerebral artery using CT imaging data, *JSME Int. J. Ser. C* 44 (2001) 982–989.
- [28] R. Torii, M. Oshima, T. Kobayashi, K. Takagi, T. Tezduyar, Influence of wall elasticity in patient-specific hemodynamics simulations, *Comput. Fluids* 36 (2007) 160–168.
- [29] R. Torii, M. Oshima, T. Kobayashi, K. Takagi, T. Tezduyar, Fluid-structure interaction modeling of a patientspecific cerebral aneurysm: influence of structural modeling, *Comput. Mech.* 43 (2008) 151–159.
- [30] H. Watanabe, S. Sugiura, H. Kafuku, T. Hisada, Multiphysics simulation of left ventricular filling dynamics using fluid-structure interaction finite element method, *Biophys. J.* 87 (2004) 2074–2085.
- [31] Q. Zhang, T. Hisada, Analysis of fluid-structure interaction problems with structural buckling and large domain changes by ale finite element method, *Comput. Methods Appl. Mech. Eng.* 190 (2001) 6341–6357.
- [32] J.S. Martín, L. Smaranda, T. Takahashi, Convergence of a finite element/ALE method for the Stokes equations in a domain depending on time, *J. Comput. Appl. Math.* 230 (2009) 521–545.
- [33] R. Lan, P. Sun, M. Mu, Mixed finite element analysis for an elliptic/mixed-elliptic coupling interface problem with jump coefficients, *Proc. Comput. Sci.* 108 (2017) 1913–1922.
- [34] R. Lan, M. Ramirez, P. Sun, Finite element analysis of an arbitrary Lagrangian-Eulerian method for Stokes/parabolic moving interface problem with jump coefficients, *Results Appl. Math.* 8 (2020) 100091.
- [35] R. Lan, P. Sun, A novel arbitrary Lagrangian-Eulerian finite element method for a parabolic/mixed parabolic moving interface problem, *J. Comput. Appl. Math.* 383 (2021) 113125.
- [36] R. Lan, P. Sun, A novel arbitrary Lagrangian-Eulerian finite element method for a mixed parabolic problem on a moving domain, *J. Sci. Comput.* 85 (2020) 9.
- [37] I. Kesler, R. Lan, P. Sun, The arbitrary Lagrangian-Eulerian finite element method for a transient Stokes/parabolic interface problem, *Int. J. Numer. Anal. Model.* (2021), in press.
- [38] R. Lan, P. Sun, A monolithic arbitrary Lagrangian-Eulerian finite element analysis for a Stokes/parabolic moving interface problem, *J. Sci. Comput.* 82 (2020) 59.
- [39] E. Weinan, B. Engquist, et al., The heterogeneous multiscale methods, *Commun. Math. Sci.* 1 (2003) 87–132.
- [40] E. Weinan, W. Ren, E. Vanden-Eijnden, A general strategy for designing seamless multiscale methods, *J. Comput. Phys.* 228 (2009) 5437–5453.
- [41] M. Amabili, *Hyperelasticity of Soft Biological and Rubber Materials*, Cambridge University Press, 2018, pp. 151–224.
- [42] C. Gasser, R. Ogden, G. Holzapfel, Hyperelastic modelling of arterial layers with distributed collagen fibre orientations, *J. R. Soc. Interface* 3 (2006) 15–35.
- [43] J. Humphrey, *Cardiovascular Solid Mechanics: Cells, Tissues, and Organs*, Springer Science & Business Media, 2013.
- [44] T. Carew, R. Vaishnav, D. Patel, Compressibility of the arterial wall, *Circ. Res.* 23 (1968) 61–68.
- [45] C. Chuong, Y. Fung, Compressibility and constitutive equation of arterial wall in radial compression experiments, *J. Biomech.* 17 (1984) 35–40.
- [46] W. Hao, S. Gong, S. Wu, J. Xu, M. Go, A. Friedman, D. Zhu, A mathematical model of aortic aneurysm formation, *PLoS ONE* 12 (2017) 2:e0170807.
- [47] D.A. Vorp, J.P. Vande Geest, Biomechanical determinants of abdominal aortic aneurysm rupture, *Arterioscler. Thromb. Vasc. Biol.* 25 (2005) 1558–1566.
- [48] D.A. Vorp, Biomechanics of abdominal aortic aneurysm, *J. Biomech.* 40 (2007) 1887–1902.
- [49] J. Zhang, J. Schmidt, E. Ryschich, H. Schumacher, J. Allenberg, Increased apoptosis and decreased density of medial smooth muscle cells in human abdominal aortic aneurysms, *Chin. Med. J.* 116 (2003) 1549–1552.
- [50] M.I. Patel, P. Ghosh, J. Melrose, M. Appleberg, Smooth muscle cell migration and proliferation is enhanced in abdominal aortic aneurysms, *Aust. N.Z. J. Surg.* 66 (1996) 305–308.
- [51] N. Airhart, B.H. Brownstein, J.P. Cobb, W. Schierding, B. Arif, T.L. Ennis, R.W. Thompson, J.A. Curci, Smooth muscle cells from abdominal aortic aneurysms are unique and can independently and synergistically degrade insoluble elastin, *J. Vasc. Surg.* 60 (2014) 1033–1041.

- [52] A.W. Chung, K. Au Yeung, G.G. Sandor, D.P. Judge, H.C. Dietz, C. van Breemen, Loss of elastic fiber integrity and reduction of vascular smooth muscle contraction resulting from the upregulated activities of matrix metalloproteinase-2 and -9 in the thoracic aortic aneurysm in Marfan syndrome, *Circ. Res.* 101 (2007) 512–522.
- [53] H. Yanagisawa, J. Wagenseil, Elastic fibers and biomechanics of the aorta: insights from mouse studies, *Matrix Biol.* 85–86 (2020) 160–172.
- [54] T. Richter, *Fluid-Structure Interactions, Lecture Notes in Computational Science and Engineering*, vol. 118, Springer International Publishing, 2017.
- [55] L. Gastaldi, A priori error estimates for the arbitrary Lagrangian Eulerian formulation with finite elements, *East-West J. Numer. Math.* 9 (2001) 123–156.
- [56] F. Nobile, L. Formaggia, A stability analysis for the arbitrary Lagrangian Eulerian formulation with finite elements, *East-West J. Numer. Math.* 7 (2010) 105–132.
- [57] T. Hughes, L. Franca, M. Balestra, A new finite element formulation for computational fluid dynamics: V. circumventing the Babuska-Brezzi condition: a stable Petrov-Galerkin formulation of the Stokes problem accommodating equal-order interpolations, *Comput. Methods Appl. Mech. Eng.* 59 (1986) 85–99.
- [58] L. Franca, T. Hughes, A.M.I. Loula, A new family of stable elements for nearly incompressible elasticity based on a mixed Petrov-Galerkin finite element formulation, *Numer. Math.* 53 (1988) 123–141.
- [59] T. Tezduyar, Stabilized finite element formulations for incompressible flow computations, *Adv. Appl. Mech.* 28 (1992) 1–44.
- [60] M. Braack, E. Burman, V. John, G. Lube, Stabilized finite element methods for the generalized Oseen problem, *Comput. Methods Appl. Mech. Eng.* 196 (2007) 853–866.
- [61] T.E. Tezduyar, S. Mittal, S. Ray, R. Shih, Incompressible flow computations with stabilized bilinear and linear equal-order-interpolation velocity-pressure elements, *Comput. Methods Appl. Mech. Eng.* 95 (1992) 221–242.
- [62] G. Scovazzi, B. Carnes, X. Zeng, S. Rossi, A simple, stable, and accurate linear tetrahedral finite element for transient, nearly, and fully incompressible solid dynamics: a dynamic variational multiscale approach, *Int. J. Numer. Methods Eng.* 106 (2016) 799–839.
- [63] N.M. Newmark, A method of computation for structural dynamics, *J. Eng. Mech. Div.* 85 (1959) 67–94.
- [64] J. Xu, K. Yang, Well-posedness and robust preconditioners for discretized fluid-structure interaction systems, *Comput. Methods Appl. Mech. Eng.* 292 (2015) 69–91.
- [65] J.A. Sethian, Fast marching methods, *SIAM Rev.* 41 (1999) 199–235.
- [66] A.G. Churbanov, P.N. Vabishchevich, Numerical solution of boundary value problems for the Eikonal equation in an anisotropic medium, *J. Comput. Appl. Math.* 362 (2019) 55–67.
- [67] J. Sethian, *Level Set Methods: Evolving Interfaces in Geometry, Fluid Mechanics, Computer Vision and Material Science*, Cambridge University Press, Cambridge, UK, 1996.
- [68] A. Friedman, W. Hao, A mathematical model of atherosclerosis with reverse cholesterol transport and associated risk factors, *Bull. Math. Biol.* (2014).
- [69] W. Hao, A. Friedman, The LDL-HDL profile determines the risk of atherosclerosis: a mathematical model, *PLoS ONE* 9 (2014) e90497.
- [70] W. Hao, E.D. Crouser, A. Friedman, Mathematical model of sarcoidosis, *Proc. Natl. Acad. Sci. USA* (2014).
- [71] H. Lee, S. Xu, Finite element error estimation for quasi-Newtonian fluid-structure interaction problems, *Appl. Math. Comput.* 274 (2016) 93–105.
- [72] M.V. De Ceniga, R. Gomez, L. Estallo, L. Rodriguez, M. Baquer, A. Barba, Growth rate and associated factors in small abdominal aortic aneurysms, *Eur. J. Vasc. Endovasc. Surg.* 31 (2006) 231–236.